NATIONAL AERONAUTICS AND SPACE ADMINISTRATION

Space Programs Summary 37-60, Vol. I

Flight Projects

For the Period September 1 to October 31, 1969

JET PROPULSION LABORATORY
CALIFORNIA INSTITUTE OF TECHNOLOGY
PASADENA, CALIFORNIA

November 30, 1969

NATIONAL AERONAUTICS AND SPACE ADMINISTRATION

Space Programs Summary 37-60, Vol. I

Flight Projects

For the Period September 1 to October 31, 1969

JET PROPULSION LABORATORY
CALIFORNIA INSTITUTE OF TECHNOLOGY
PASADENA, CALIFORNIA

November 30, 1969

SPACE PROGRAMS SUMMARY 37-60, VOL. I

Prepared Under Contract No. NAS 7-100
National Aeronautics and Space Administration

Preface

The Space Programs Summary is a multivolume, bimonthly publication that presents a review of technical information resulting from current engineering and scientific work performed, or managed, by the Jet Propulsion Laboratory for the National Aeronautics and Space Administration. The Space Programs Summary is currently composed of four volumes:

Vol. I. *Flight Projects* (Unclassified)

Vol. II. *The Deep Space Network* (Unclassified)

Vol. III. *Supporting Research and Advanced Development* (Unclassified)

Vol. IV. *Flight Projects and Supporting Research and Advanced Development* (Confidential)

Contents

PLANETARY–INTERPLANETARY PROGRAM

I. *Mariner* Mars 1969 Project

PLANETARY–INTERPLANETARY PROGRAM

A. Project Description and Status

1. Description

The primary objective of the *Mariner* Mars 1969 Project is to make two flyby exploratory investigations of Mars in 1969, which will set the basis for future experiments—particularly those relevant to the search for extraterrestrial life. The secondary objective is to develop Mars mission technology.

The spacecraft design concept was modeled after the successful *Mariner IV* spacecraft, considerably modified to meet the 1969 mission requirements and to enhance mission reliability.

The launch vehicle was the *Atlas/Centaur* SLV-3C, the same as used for the *Surveyor* missions. This vehicle, developed by General Dynamics/Convair Company for the Lewis Research Center, has single- or double-burn capability in its second stage and a considerably increased performance rating over the *Atlas D/Agena D* used in the *Mariner IV* mission.

The *Mariner* Mars 1969 mission has been and is supported by the Deep Space Network (DSN) and other NASA facilities.

The six planetary-science experiments selected by NASA for the *Mariner* Mars 1969 missions are listed in Table 1.

2. Project Status

With the Mars encounter successfully completed and all Mars data returned, the *Mariner* Mars 1969 Project has concentrated in three areas: (1) science data reduction, analysis, and reporting; (2) post-encounter spacecraft testing and scientific operations; and (3) study and planning of possible long-term future experimental operations with the two *Mariner* spacecraft.

Early interpretation efforts of the experiment teams have been reported in *Science* (August, September, and October 1969 issues) and at various scientific meetings. Television pictures, spectra, and other instrumental data

Table 1. *Mariner* Mars 1969 science experiments and investigations

Experiment	Investigator	Affiliation
Television	R. B. Leighton[a]	CIT
	B. C. Murray	CIT
	R. P. Sharp	CIT
	N. H. Horowitz	CIT
	A. G. Herriman	JPL
	R. K. Sloan	JPL
	M. E. Davies	Rand Corp.
	C. Leovy	University of Washington
	B. A. Smith	New Mexico State University
Infrared spectrometer	G. C. Pimentel[a]	UCB
	K. C. Herr	UCB
Ultraviolet airglow spectrometer	C. A. Barth[a]	University of Colorado
	F. C. Wilshusen	University of Colorado
	K. Gause	University of Colorado
	K. K. Kelly	University of Colorado
	R. Ruehle	University of Colorado
	J. B. Pearce	University of Colorado
	E. F. Mackey	Packard-Bell Electronics Corp.
	W. G. Fastie	Johns Hopkins University
Infrared radiometer	G. Neugebauer[a]	CIT
	G. Munch	CIT
	S. C. Chase	Santa Barbara Research Center, Hughes Aircraft Co.
S-band occultation	A. J. Kliore[a]	JPL
	G. Fjeldbo	Stanford University/JPL
	S. I. Rasool	Goddard Institute of Space Studies
Celestial mechanics	J. D. Anderson[a]	JPL
	W. L. Martin	JPL

[a]Principal investigator.

continued to be processed and studied (the image-processing laboratory TV effort is expected to continue well into 1970). Trajectory and instrument-pointing calculations, essential to the scientific interpretations, continued to be refined during the period, and cartographic work was begun.

A thorough engineering investigation of the *Mariner VII* flight anomaly of July 30 and 31, involving many equipment tests as well as the analysis of flight data, was conducted during the period. The hypothesis that the anomaly was caused by a meteorite impact was apparently ruled out by doppler data, which showed no disturbance of the spacecraft as much as a minute after the outbreak of electrical violence. Tests of the *Mariner VI* and *Mariner VII* radio subsystems showed the two radios to be in satisfactory and stable condition, and the anomalous conditions observed earlier in flight were not repeated.

A number of operations used the instruments designed for close-up observation of Mars to study the sky. Ultraviolet and infrared sky surveys and galactic observations and an ultraviolet scan of Comet 1969-B have been performed. In addition, a television calibration survey included narrow-angle pictures of specific stars.

A test of the general theory of relativity, using the *Mariner VI* and *Mariner VII* spacecraft as they approach superior conjunction or syzygy with the sun, has been proposed. This experiment would require prolonged doppler and ranging tracking to determine the post-encounter trajectory precisely, and a series of ranging passes to measure the retardation of the tracking signal by the solar gravitational field. This should provide the most conclusive experimental verification to date of the theory. Pending formal NASA approval of the operations, plans and studies are under way on implementation modes. Weekly ranging passes were conducted during the report period.

The *Mariner* Mars 1969 mission, as originally defined, was scheduled to conclude on November 1, 1969.

B. Guidance and Control

1. Solar-Panel Array Performance

The *Mariner VI* and *VII* solar-panel arrays have completed their flight performance successfully. Four solar panels were utilized on each spacecraft to provide the primary electrical power. The combined surface area of the four panels totaled 83 ft^2 on which 17,472 2 × 2 cm *N* on *P*-type silicon solar cells were mounted. The four panels weighed 112 lb and generated approximately 475 W of electrical power at Mars encounter. The electrical configuration of each array consists of 78 cells connected in series and 224 cells connected in parallel and laid out into 24 isolated electrical sections.

The flight performance characteristics of the solar panels are extrapolated from information accumulated from telemetry data. Voltage and current outputs of individual panels were recorded and calculated to generate panel performance data points at spacecraft loads. When these data points were evaluated against the predicted power curve, it indicated that the *Mariner* array flight power performance was within 1% of the nominal predicted performance. The predicted power performance was based on actual electrical measurements made

on the panels at Table Mountain test site. Two temperature transducers were employed and were located on the back side of one of the four panels for monitoring array temperature. The transducer data indicate that the flight panels were measuring approximately 3°C colder than anticipated. They also indicated as expected that the inboard section of the panels (closest to the spacecraft) were warmer than the outboard section by approximately 4°C.

To aid in the evaluation of the array performance, an I_{sc}–V_{oc} transducer was mounted on one panel. The transducer is a network of three solar cells mounted on a circuit board and located on the front side of the panel. Measurements of the short-circuit currents of two cells were made and provided information relative to the power degradation of the panels by radiation or other environments. The third cell which provides temperature-dependent output (open-circuit voltage) was used to aid in evaluating the thermal equilibrium characteristics of the array. Correlation of the telemetry data of the transducer output to the solar array indicated that at encounter the solar array may have been 5% lower in output than predicted before launch. Three percent of the loss was apparently due to radiation damage and the rest of the loss due to other causes, including prediction accuracy.

In summary, the solar arrays of the *Mariner VI* and *Mariner VII* have provided power to the spacecraft throughout the mission except during launch, before sun acquisition, and during midcourse maneuver. The solar panel components sustained the launch, cruise, and Mars encounter without apparent anomaly.

II. *Mariner* Mars 1971 Project

PLANETARY–INTERPLANETARY PROGRAM

A. Project Description and Status

1. Description

The primary objective of the *Mariner* Mars 1971 Project is to place two spacecraft in orbit around Mars that will be used to perform scientific experiments directed toward achieving a better understanding of the physical characteristics of that planet. Principal among these experiments are measurements of atmospheric and surface parameters at various times and locations to determine the dynamic characteristics of the planet. Approximately 70% of the Martian surface will be observed during a minimum of 90 days of orbital operations.

During Mission A, it is planned to map the topography of a large portion of the Martian surface at a resolution significantly higher than that achievable with earth-based methods or by the *Mariner* Mars 1969 spacecraft. In addition, measurements will be made of the composition, density, pressure, and thermal properties of the planet's atmosphere. Other measurements will be directed toward an understanding of Mars' surface temperatures, composition, and thermal properties (particularly at the polar caps); its apparent lack of internal activity; its mass distribution; and its shape.

During Mission B, data will be sought on time-variable features of the Martian surface associated with the wave of darkening wherein both seasonal and secular changes occur. Also, information on atmospheric structure and gross dynamics will be obtained, as well as information directed toward an understanding of Mars' mass distribution, its shape, and its apparent lack of internal activity.

A capability will exist to redirect goals for either mission to the alternate mission if desired. The two launches are anticipated for May 1971, with arrival at the planet during the following November.

An engineering objective of the project is to demonstrate the ability of the spacecraft to perform orbital operations in an adaptive mode wherein information from one orbital pass is used to develop the operations plan for subsequent orbital passes. Studies indicate a high probability that at least one of the spacecraft will survive the sun occultation period which occurs shortly after the 90-day mission is

completed. This makes it possible to conduct an Extended Mission for about a year after orbit insertion. The Extended Mission will probably consist of one or two data taking sequences per week with the capability of recording and playing back about a half-recorder of data (16 TV frames and 11 min of spectrometer data).

One of the *Mariner* Mars 1971 flight spacecraft will be new, and the other will be the spare flight spacecraft of the *Mariner* Mars 1969 Project modified to meet the requirements of the 1971 missions and to enhance mission reliability. The proof test model spacecraft of the *Mariner* Mars 1969 Project will be modified to become the proof test model for the *Mariner* Mars 1971 Project, to be used for preliminary testing and as a simulator in support of flight operations. A major modification for the *Mariner* Mars 1971 mission will be the addition of a rocket motor required to decelerate the spacecraft and place it in orbit around Mars.

Separate scientific instrument subsystems will be required to accomplish the television, infrared radiometer, ultraviolet spectrometer, and infrared spectrometer interferometer experiments given in Table 1. The S-band occultation and celestial mechanics experiments will require no additional equipment on the spacecraft.

Table 1. *Mariner* Mars 1971 scientific experiments and principal investigators

Television	
H. Masursky	Team leader
H. Masursky	PI/U.S. Geological Survey
R. Batson	CI/U.S. Geological Survey
W. Borgeson	
M. Carr	
J. F. McCauley	
D. Milton	
R. Wildey	
D. Wilhelms	
J. Lederberg	PI/Stanford University
E. Levinthal	CI/Stanford University
J. B. Pollack	CI/Cornell University
C. Sagan	CI/Cornell University
G. de Vaucouleurs	PI/University of Texas
W. B. Thompson	PI/Bellcomm
G. A. Briggs	CI/Bellcomm
P. L. Chandeysson	CI/Bellcomm
E. N. Shipley	CI/Bellcomm
B. Smith	PI/New Mexico State University
M. E. Davies	CI/Rand Corp.
W. K. Hartmann	CI/Arizona State University
N. H. Horowitz	CI/Caltech
R. B. Leighton	CI/Caltech
C. B. Leovy	CI/University of Washington
T. B. McCord	CI/MIT
B. C. Murray	CI/Caltech
R. P. Sharp	CI/Caltech

Ultraviolet spectrometer	
C. Barth	PI/University of Colorado
C. W. Hord	CI/University of Colorado
J. B. Pearce	CI/University of Colorado

Infrared interferometer spectrometer	
R. A. Hanel	PI/Goddard Space Flight Center
B. J. Conrath	CI/Goddard Space Flight Center
W. A. Hovis	CI/Goddard Space Flight Center
V. Kunde	CI/Goddard Space Flight Center
G. V. Levin	CI/Biospherics
P. D. Lowman	CI/Goddard Space Flight Center
C. Prabhakara	CI/Goddard Space Flight Center
B. Schlachman	CI/Goddard Space Flight Center

Infrared radiometer	
G. Neugebauer	PI/Caltech
S. C. Chase	CI/Santa Barbara Research Center
E. D. Miner	CI/JPL
G. Munch	CI/Caltech

Celestial mechanics	
J. Lorell	Team leader
J. Lorell	PI/JPL
J. D. Anderson	CI/JPL
W. L. Martin	CI/JPL
W. L. Sjogren	CI/JPL
I. Shapiro	PI/MIT

S-band occultation	
A. Kliore	PI/JPL
D. L. Cain	CI/JPL
G. Fjeldbo	CI/JPL
B. L. Seidel	CI/JPL

PI = Principal investigator, who is the proposer for each experiment.

CI = Co-investigator, who assists the proposer on each experiment.

Team leader heads a particular group of PIs and CIs on an experiment where there is more than one PI.

Management responsibilities for the overall project, the Spacecraft System, the Mission Operations System, and the Tracking and Data System have been assigned to JPL. Lewis Research Center has been assigned management responsibility for the Launch Vehicle System. The launch vehicle will be an *Atlas/Centaur* developed by General Dynamics/Convair.

The *Mariner* Mars 1971 missions will be supported by the Air Force Eastern Test Range launch facilities at Cape Kennedy, the tracking and data acquisition facilities of the Deep Space Network, and other NASA facilities.

2. Status

The *Mariner* Mars 1971 Project Plan has been reviewed and approved, subject to a list of changes requested by the Director of Planetary Programs of the Office of Space Science and Applications. No major changes are necessary in the science objectives or in the instrument hardware.

Table 1 gives a complete list of principal investigators for the science experiments. The principal investigators who submitted experiment proposals using television imagery have regrouped to form the photointerpretation team (Fig. 1). The team leader will furnish recommendations for television equipment fabrication, testing, calibration, and for mission operations (including orbital trajectory parameter selection and image processing).

The spacecraft system detail reviews of all subsystems have been completed. The final design is shown in Fig. 2. Freeze dates are now being established for each subsystem, and the overall schedule will be completed by November 15. All major subsystem contracts have been drawn up.

The IBM 7044 and 7094 computers will be replaced with two IBM 360/75 computers, which will be coupled to a dual processor Univac 1108.

DSN simulation system capabilities have been modified to meet project requirements. Direct high-rate (video) data from DSS 14 to the SFOF will be provided, and no high-speed data demultiplexers will be provided at the Ground Support Facility/mission test computer interface.

An uprated *Atlas* will be used for the mission. The booster engine thrust will be increased from 336,000 to

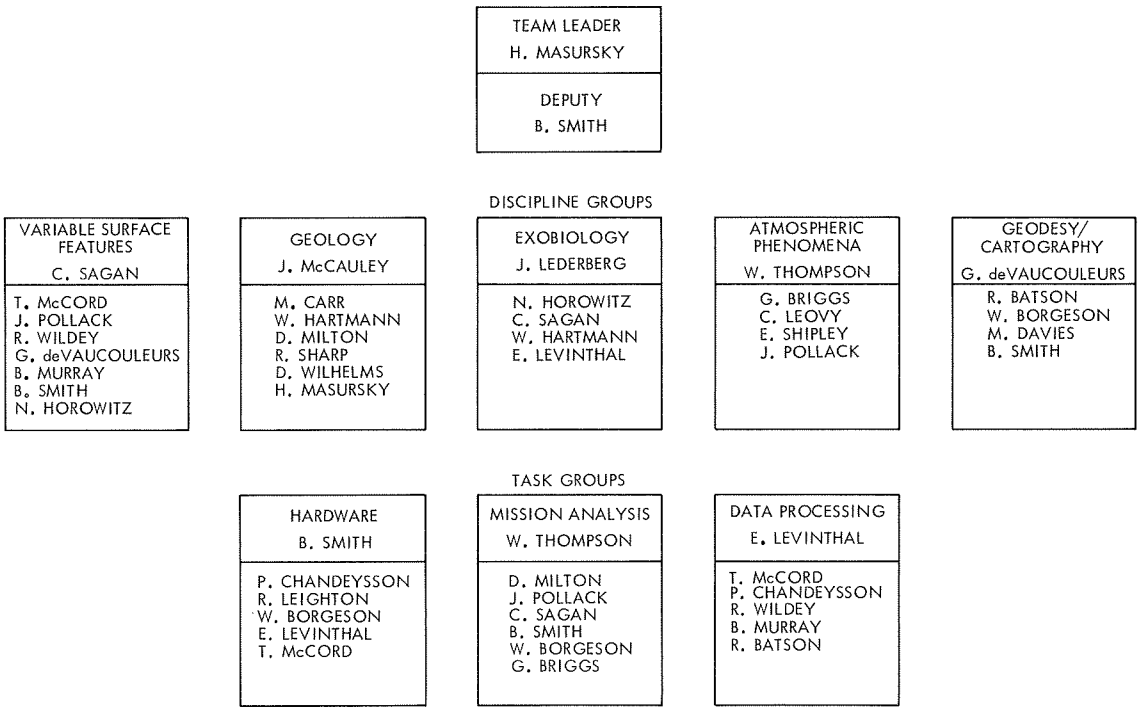

Fig. 1. Television team matrix

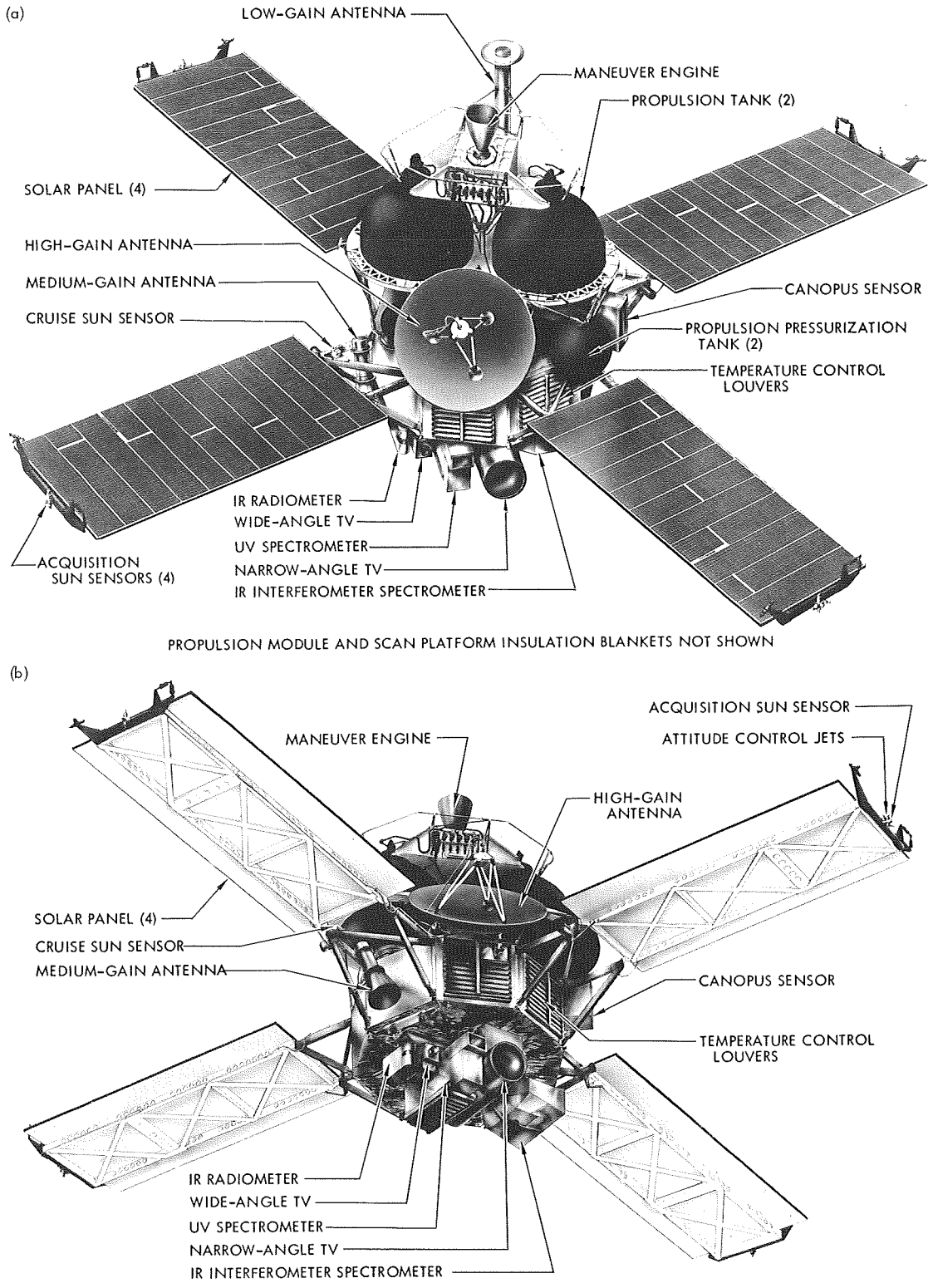

Fig. 2. Final *Mariner* Mars 1971 spacecraft configuration: (a) top view, (b) bottom view

342,000 lb, and the sustainer engine thrust from 58,000 to 60,000 lb. The AFETR Range Safety Office has approved the concept for the inflight spacecraft propellant dispersion system. The destruct system, which is similar to that used for the *Surveyor* missions, will use two shaped charges, one for each propellant tank, mounted on the outer periphery of the *Centaur* forward equipment shelf and firing throughout the thermal bulkhead for rupture of the propellant tanks.

B. Guidance and Control

1. Optical Sensors

The optical sensors for the *Mariner* Mars 1971 spacecraft are basically the same as those on the *Mariner* Mars 1969 spacecraft with minor modifications to minimize the effects of reflected light from Mars during orbit.

a. Sun sensors. The sun sensors provide the position-sensing elements in the pitch and yaw acquisition and cruise attitude-control loops. Acquisition sensors in conjunction with cruise sensors provide a complete sphere field of view for initial sun acquisition. The cruise sensors provide pitch and yaw position-error signals for cruise limit cycle operation after acquisition. The sun gate indicates sun acquisition to the attitude-control logic when the sun is within the sun gate sensor's conical field of view.

Two potential problems may arise from Mars reflected light. First, the Mars lit limb can cause an angular offset in pitch and yaw if it is bright enough and close enough to the cruise sensor's field of view. The problem is more severe for the lower-inclination orbits of those being considered. Figure 3 illustrates the variations of Mars illuminance versus spacecraft cone angle for a low orbit inclination of 60 deg. The cone angle of an object is the angle between the spacecraft–sun line and the spacecraft–object line. Fortunately, the closer the planet is to the cruise sun sensor's field of view (i.e., smaller planet cone angle), the smaller the lit crescent becomes. Also for the orbits being considered, smaller planet cone angles tend to occur near apoapsis (where the planet is furthest away) and, therefore, appears dimmer. Redesign of cruise sensor baffling will eliminate the offset problem for limb cone angles greater than 20 deg. For smaller angles, the planet is fairly dim compared to the sun, and the offset is minimized.

The second potential problem arises when the spacecraft is reacquiring the sun after a maneuver near the

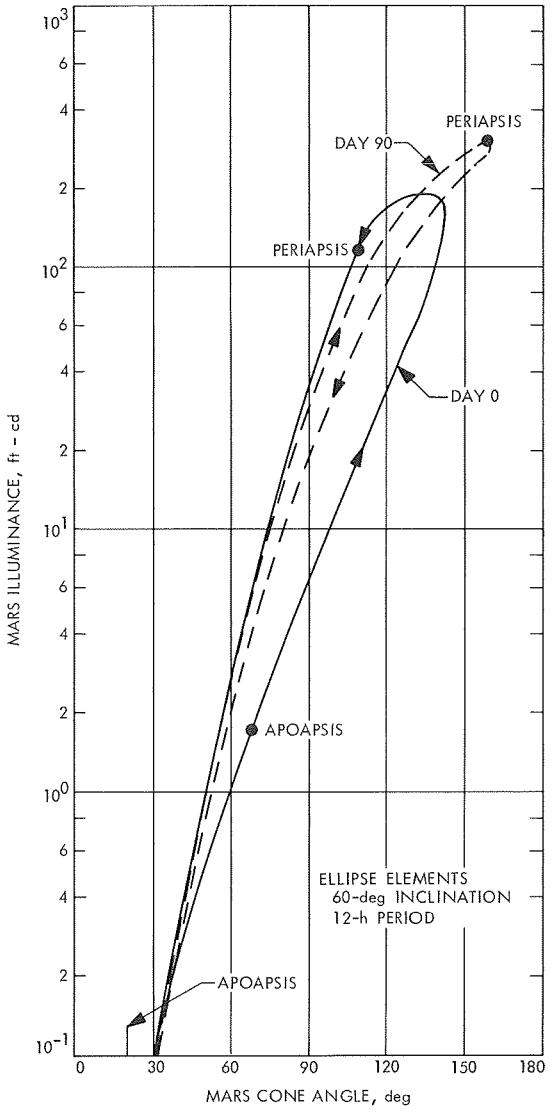

Fig. 3. Mars illuminance versus cone angle

planet. Since all sun sensors are energized, reflected light from the planet onto the acquisition sensors can cause a shift in the position null and delay the occurrence of the sun gate. This is particularly true at reacquisition from the orbit insertion or the period correction trim maneuvers which occur at periapsis where the planet appears very bright. As shown in Fig. 3, peak illuminance due to planet reflected light is approximately 300 ft-cd. (The sun at Mars' distance is approximately 5500 ft-cd.) This problem will be minimized by scale factor changes to the sensors.

b. Canopus sensor and stray-light. The Canopus sensor provides position-error information to stabilize the spacecraft about the roll axis. Intensity information

is also provided to assure that the sensor has acquired the correct star, Canopus.

Functional changes to the Canopus sensor for *Mariner* Mars 1971 are minimal. One change being mechanized is associated with reacquiring Canopus after possible stray-light interference from the planet. Normally the roll axis will be placed on inertial control during these periods, but the Canopus sensor will remain energized. In this condition the sensor can internally track Canopus within its total roll field of view without affecting the spacecraft roll attitude. Should the sensor be confused by stray-light, it will lose the Canopus acquisition signal even though Canopus has not passed out of the field of view. When normal optical control is restored, a complete 360-deg roll search will be initiated. To avoid this unnecessary roll, a search for Canopus by the sensor within its total roll field of view (a "flyback and sweep" search) is performed prior to reestablishing normal optical control.

There are two modes in orbit when stray-light from the planet can cause interference with the Canopus sensor. During normal optical control, a lit portion of the planet may fall within the Canopus sensor's stray-light field of view. This field of view is currently defined as $\pm 15 \times \pm 33$ deg. Roll inertial control must be used whenever a lit portion of the planet is within this field of view. Figure 4 shows the trace of the near-horn motion of the planet across the Canopus sensor's stray-light field of view for an 80-deg inclination orbit for various days in orbit. The coordinate system is centered on the mechanical null axis of the sensor. The parameter which most affects these plots is orbital inclination. Indeed, for the 60-deg inclination orbit, no violations occur at all. Violations first occur when the inclination reaches about 63 deg.

During reacquisition of Canopus after a maneuver, the planet may enter the Canopus sensor's roll search field of view. This is the field of view swept out by the sensor's active field of view as the spacecraft performs a complete roll. Several different orbits were examined. The planet was within the roll search field of view at periapsis where reacquisition from the orbit insertion and the period correction orbit trim maneuvers occur. Although not bright enough to damage the sensor, the planet would be acquired at several points across its diameter. At apoapsis (where the periapsis trim maneuver occurs), though not in the active sensor field of view, the planet enters the stray-light field of view (extending from 57 to 123 deg in the cone) during roll search and a problem results.

The method of solving these problems is to utilize the information storage and programmable aspects of the on-board central computer and sequencer (CC&S). During cruise, the times at which the planet enters and exits the stray-light field of view can be programmed into the CC&S so that roll inertial control can be established. This program would be based on the best orbital elements known at that time and would typically look like a straight line approximation of Fig. 5. The program would be updated occasionally to account for uncertainties or perturbations in the orbit which would affect the timing. For reacquisitions after maneuvers, the CC&S would perform the inverse of the spacecraft maneuver turns so that no roll search would be required. Ground commands are available to backup the CC&S functions. Commands are also available to aid reacquisition should Canopus acquisition be unintentionally lost.

2. Roll Error Canopus Acquisition (RECA)

a. Introduction. The *Mariner* Mars 1969 flight has pointed out that a significant improvement in the attitude-control system (ACS) performance for a non-standard mode can be implemented. These changes to the ACS, when in the DC 15 mode, have been mechanized in the *Mariner* Mars 1971 attitude-control electronics and are described herein.

b. Mariner Mars 1969 mechanization. During the cruise mode of the spacecraft, control about the roll axis is maintained by referencing the spacecraft to the star Canopus. This is accomplished through the usage of a Canopus tracker as part of the ACS. The ACS effects closed-loop positional control, maintaining Canopus about the null axis of the Canopus tracker. The Canopus tracker has three outputs:

(1) Roll error output. Provides a voltage proportional to the displacement of the star from the center of the tracker's field of view.

(2) Brightness. Provides a voltage proportional to the brightness of the star within its field of view.

(3) Canopus acquisition (CA). Provide a logic-type signal (1 or 0) to indicate whether the star of proper brightness is within its field of view.

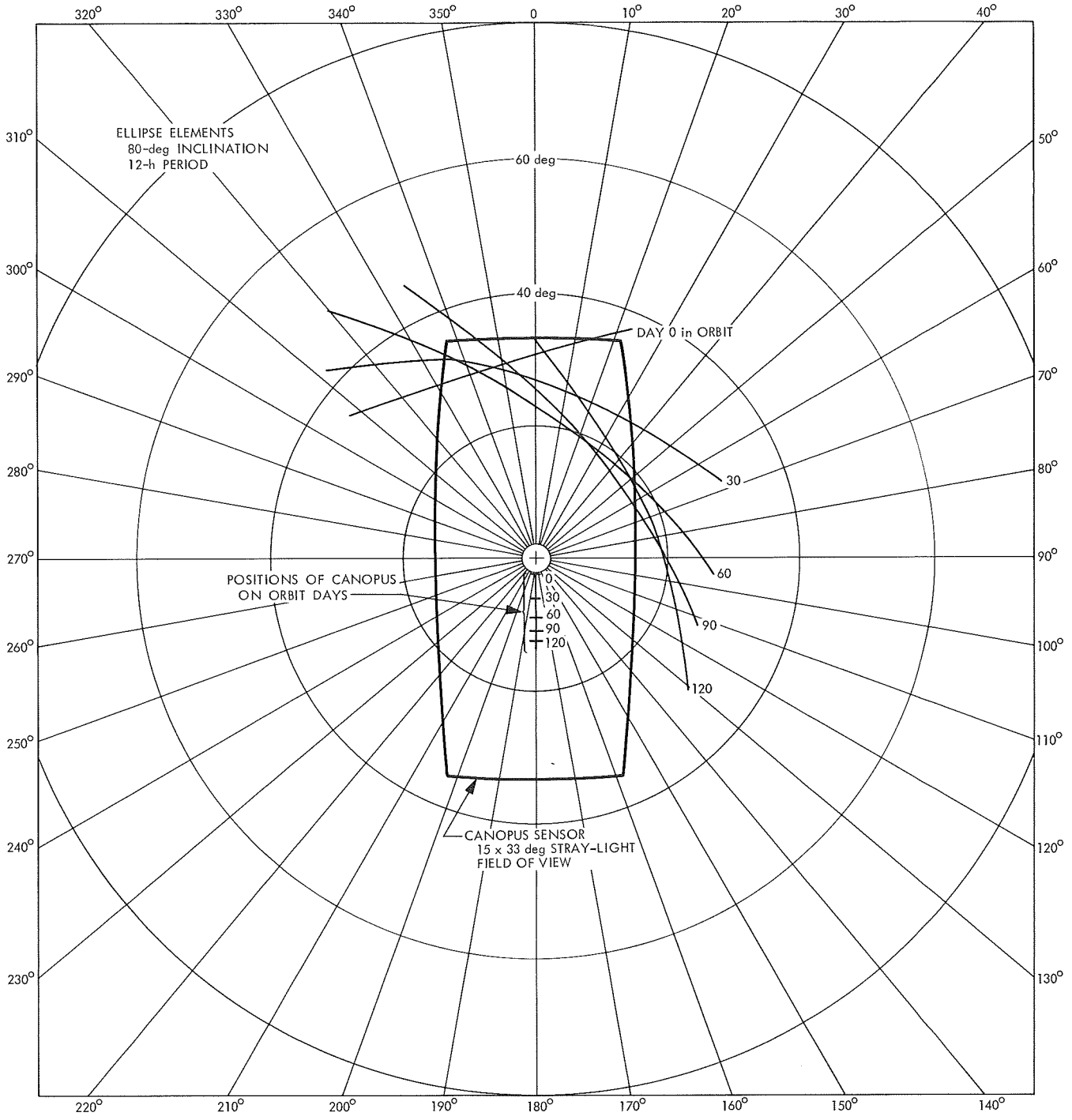

Fig. 4. Trace of planet's near horn across Canopus sensor stray-light field of view

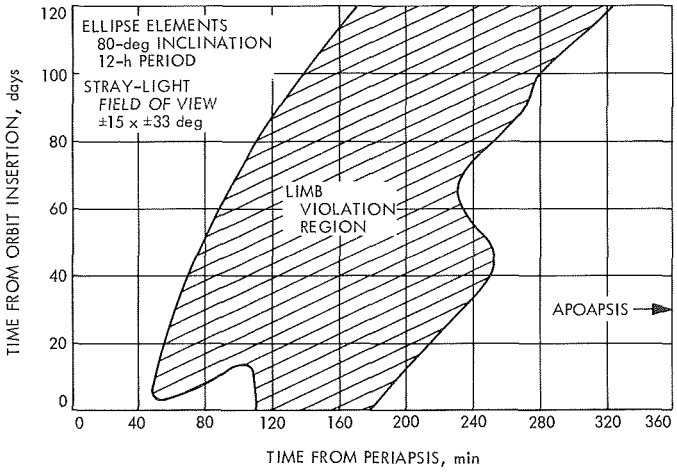

Fig. 5. Time of stray-light field of view violations versus days in orbit

The tracker is further characterized by the presence of low and high brightness gates that are used to discriminate against the acquisition of luminous bodies with different brightness properties than Canopus. DC 15, a ground transmitted backup command, has the property of disabling these gates, affording the tracker the capability of tracking objects as low as 0.02 × Canopus intensity and upward. In the DC mode, when tracking objects of lower intensity than that defined by the low brightness gate, the CA output of the tracker does not go true.

In a standard mission sequence, the signal CA is used to turn the roll gyros off and enable the derived rate feedback about the switching amplifiers. This conserves power by turning off the gyros and, since gyros have a finite lifetime, extends their usefulness in terms of total mission time. The derived rate feedback provides a pseudorate suitable for rate damping required to maintain control-loop stability.

The GPWR (gyro power on) logic equation, as mechanized on the *Mariner* Mars 1969, contains the terms relevant to this discussion as follows:

$$\text{GPWR} = \ldots\ldots\ldots + \overline{\text{CA}} \cdot \overline{\text{DC15}} + \ldots\ldots\ldots \quad (1)$$

This maintains the gyros on for CA = 0 provided DC 15 = 0. For DC 15 = 1, the CA signal does not exercise control over the GPWR equation.

The inherent shortcoming of Eq. (1) is that, in effect, it states that should the system be in the DC 15 mode ($\overline{\text{DC15}}$ = 0), the gyros shall remain shut off regardless of whether or not the tracker has a luminous body within its field of view.

c. Mariner Mars 1971 mechanization. A simple change has been implemented on the *Mariner* Mars 1971 with resultant improved system performance in the DC 15 mode. Since the problem is that the tracker can track objects without concurrent indication on the CA line when in the DC 15 mode, the attitude-control electronics operates on the roll error output line, generating a synthetic CA signal termed RECA.

Figure 6a shows the circuit and logic mechanization. In Fig. 6a the 2N2222 is normally kept in an *on* position causing $\overline{\text{RECA}}$ = 0, until the roll error voltage becomes more negative than approximately −10 V. For that condition, corresponding to the absence of an object within the tracker's field of view, the 1N754A zener diode is broken down and the 2N2222 is turned off, causing $\overline{\text{RECA}}$ = 1. Figure 6b shows a partial logic implementation of the GPWR equation. Again, as in Eq. (1), an incomplete form of the equation is

$$\text{GPWR} = \ldots\ldots\ldots + \overline{\text{CA}} \cdot (\overline{\text{DC15}} + \overline{\text{RECA}}) + \ldots\ldots\ldots \quad (2)$$

This causes the gyros to be shut off when in the DC 15 mode only in the presence of RECA (assume that CA = 0) and results in an automatic gyro turn-on when in the

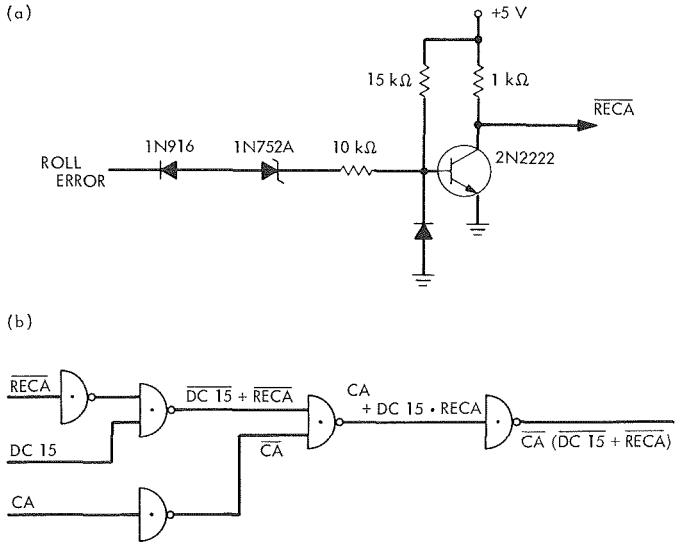

Fig. 6. Roll error Canopus acquisition: (a) circuit and logic mechanization, (b) partial logic implementation of GPWR equation

DC 15 mode if the roll error signal goes to the roll-search level.

3. Derived Rate Parameters Optimization

a. Introduction. A thorough study of the derived rate parameters[1] optimization in the *Mariner* Mars 1971 attitude-control system is presented. The derived-rate parameters were optimized under the following considerations:

(1) To provide an adequate noise guard for the undisturbed limit cycle mode.

(2) To minimize the derived-rate steady-state error (hangoff) under constant disturbing torques.

(3) To maximize the convergent rate from a fairly large initial rate or position offset to the normal limit cycle mode.

Analytical methods and digital computer simulation techniques were used to obtain the results.

b. Derived rate attitude-control system configuration. A single-axis attitude-control system is shown in Fig. 7. The angular position of the vehicle is measured by a position sensor (i.e., sun sensor). The output of the sensor is a voltage E_p that is linearly proportioned to the angular position θ, provided θ is small ($\theta \leq 2$ deg). The sensor output is summed with the derived rate feedback E_d to produce an error signal ϵ. This error signal drives a switching amplifier with a deadband $2\theta_{db}$ and minimum on-time t_{on}. The deadband width is determined by the attitude-control accuracy requirement of the mission. The minimum on-time is determined by the thrust profile. The output of the switching amplifier is used to operate the solenoid valves which, in turn, control the gas jets and generate the proper control torque.

The "derived rate" is basically a phase lag network with transfer function $K_d/(\tau s + 1)$. In hardware design, τ is equal to τ_c when the switching amplifier is on (charge) and equal to τ_d with $\tau_d > \tau_c$ when the switching amplifier is off (discharge). The function of the derived rate feedback is to provide an adequate damping in the attitude-control system.

c. Parameters optimization

Hardware constraints. The hardware design of *Mariner* Mars 1971 attitude-control system is shown in Fig. 8 where the two switching amplifiers have threshold currents set to be +5 and −5 μA. R_s is the sun-sensor input resistor and is chosen to be 200 kΩ. This value is determined by allowing a 5-A current flow through the resistor when the position error is equal to θ_{db}. Then θ_{db} is chosen to be 0.25 deg (4.36 mrad) and the sun sensor characteristic curve shown in Fig. 9 is used to convert this angle to the corresponding position signal.

The operation of the circuit will now be summarized. When the switching amplifier is on (assume it to be +5 μA), a voltage of 26 V would be applied to diode CK1 and would charge the capacitor C through the diode CK1, the zener diode CK3, and the resistor R_1. The 8-V zener diodes CK3 and CK4 are used to isolate the two different polarity amplifiers. If the capacitor voltage E_d is less than 8 V, CK4 will not conduct. Thus one constraint in the circuit design is that the absolute value of E_d should never exceed 8 V. The equivalent charging and discharging circuitry is shown in Fig. 10. The calculation of E is based on an 8 V zener diode drop and 0.7 V drop across the silicon diode CK1, or

$$E = E_{supply} - 8.0 - 0.7$$
$$= 26 - 8.0 - 0.7 = 17.3 \text{ V} \quad (1)$$

[1]Crawford, W., *Mariner '71 Switching Derived Rate Test Results*, May 13, 1969 (JPL internal document).

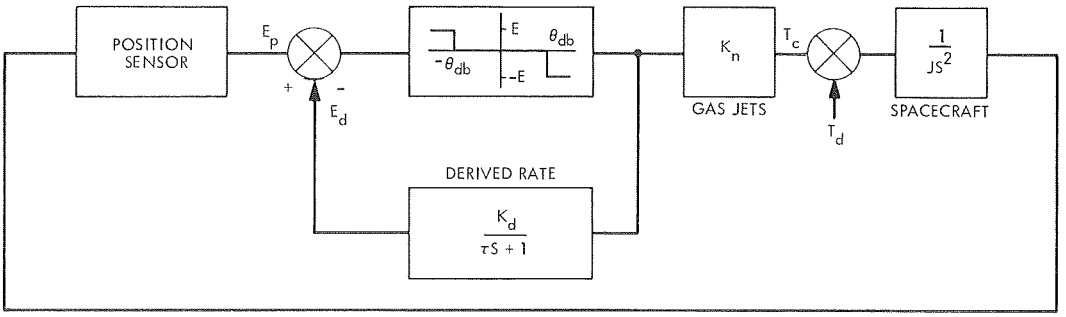

Fig. 7. A single-axis attitude-control system

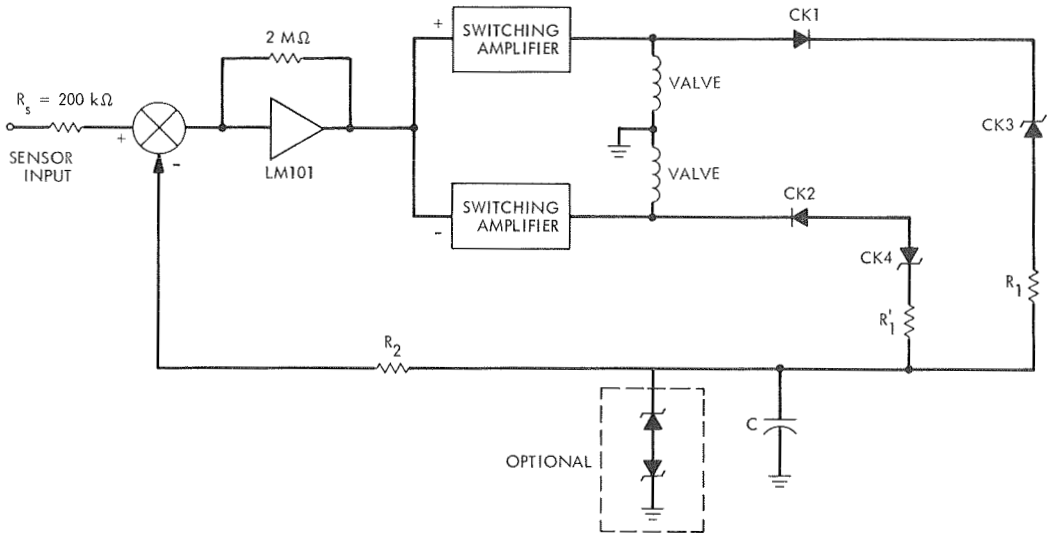

Fig. 8. Hardware design of *Mariner* Mars 1971 attitude-control system

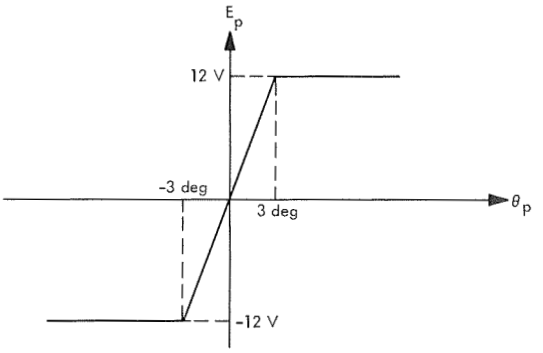

Fig. 9. Sun sensor characteristic curve

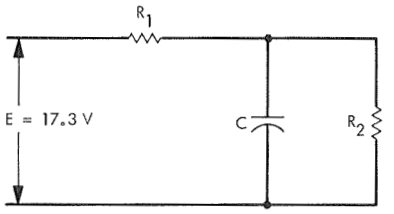

Fig. 10. Equivalent charging and discharging circuitry

The charging time constant τ_c and discharging time constant τ_d are given by

$$\tau_c = \frac{R_1 R_2}{R_1 + R_2} C \tag{2}$$

and

$$\tau_d = R_2 C \tag{3}$$

The maximum charging voltage across the capacitor is determined by

$$E_{\max} = \frac{E R_2}{R_1 + R_2} \tag{4}$$

Since it is desirable to generate a feedback signal for all possible position errors, a second constraint on the hardware design would be

$$\frac{E_{\max}}{R_2} \geq \frac{E_s}{R_s} \tag{5}$$

where E_s is the saturation voltage of the sun sensor characteristic curve and is designed to be 12 V.

Analytical solution and computer results. In this section the parameters (R_1, R_2 and C) are selected, subject to the hardware constraints and performance considerations previously described.

We obtain the following two conditions:

$$E_d \text{ (maximum)} = \frac{E_s}{R_s} R_2 \leq 8$$

or

$$R_2 \leq \frac{8 \times 200 \times 10^3}{12} = 133.5 \text{ k}\Omega \tag{6}$$

From Eqs. (4) and (5)

$$\frac{E}{R_1 + R_2} \geq \frac{E_S}{R_S}$$

or

$$R_1 + R_2 \leq \frac{17.3 \times 200 \times 10^3}{12} = 288\ \text{k}\Omega \tag{7}$$

From noise protection consideration, it is desired to have a noise guard of a certain level and maintain that level for all ω_r greater than a certain value (e.g., 5 μrad/s). Here ω_r is the return rate of the spacecraft toward the deadband. By selecting the noise guard to be 0.2 μA (0.010 deg) we obtain

$$\frac{E_{\max} t_{\text{on}}}{\tau_c R_2} \exp\left(-\frac{t}{R_2 C}\right) + k\omega_r t \geq 0.2 \times 10^{-6} \tag{8}$$

or

$$\frac{E\, t_{\text{on}}}{R_1 R_2 C} \exp\left(-\frac{t}{R_2 C}\right) + k\omega_r t \geq 0.2 \times 10^{-6} \tag{9}$$

for all t where $k = 1.145 \times 10^{-3}$ is the proportional constant calculated from the sun sensor characteristic curve. By differentiating the left side of Eq. (9) its minimum value is found to be at

$$t = -R_2 C \ln \frac{k\omega_r (R_2 C)^2 R_1}{E\, t_{\text{on}}} \tag{10}$$

Substituting Eq. (10) into Eq. (9), we have

$$k\omega_r R_2 C \left[1 - \ln \frac{k\omega_r (R_2 C)^2 R_1}{E\, t_{\text{on}}}\right] \geq 0.2 \times 10^{-6} \tag{11}$$

Also by letting $t = 0$ Eq. (9) reduces to

$$\frac{E\, t_{\text{on}}}{R_1 R_2 C} = 0.2 \times 10^{-6} k_1, \quad k_1 \geq 1 \tag{12}$$

Since it is desirable to have a higher noise protection level during amplifier switching, k_1 is chosen to be greater than 1.25. Substituting this result into Eq. (11), we obtain

$$1 + \ln 1.25 - \ln \frac{k\omega_r R_2 C}{0.2 \times 10^{-6}} > \frac{0.2 \times 10^{-6}}{k\omega_r R_2 C} \tag{13}$$

The above condition can be satisfied if

$$0.55 \leq \frac{k\omega_r R_2 C}{0.2 \times 10^{-6}} \leq 2.12 \tag{14}$$

or

$$19.25 \leq R_2 C \leq 74.2$$

Equations (12) and (14) are the sufficient conditions for the condition represented by Eq. (11) to be true. Thus, a third constraint in system design is

$$R_1 R_2 C \leq \frac{17.3 \times 20 \times 10^{-3} \times 1.25}{0.2 \times 10^{-6}} = 2162 \times 10^3$$

and

$$19.25 \leq R_2 C \leq 74.2$$

Another consideration in selecting the values of the parameters (R_1, R_2 and C) would be that the maximum position error should be within a certain limit (e.g., 0.5 deg) for a constant disturbing torque no larger than a certain value (e.g., 15,000 dyne-cm). The maximum derived rate hangoff was derived[2] as

$$E_d \cong \frac{E_{\max}}{1 + \dfrac{T_c \tau_c}{T_d \tau_d}} \left(1 - \frac{T_c\, t_{\text{on}}}{T_d \tau_d}\right) \tag{15}$$

Using the relations in Eqs. (2) to (4), Eq. (15) can be rewritten as

$$E_d \cong \frac{\dfrac{E R_2}{R_1 + R_2}}{1 + \dfrac{T_c R_1}{T_d (R_1 + R_2)}} \left(1 - \frac{T_c\, t_{\text{on}}}{T_d R_2 C}\right) \tag{16}$$

To satisfy the maximum position error constraint, we achieve the following inequality

$$\frac{\dfrac{E R_2}{R_1 + R_2}}{1 + \dfrac{T_c R_1}{T_d (R_1 + R_2)}} \left(1 - \frac{T_c\, t_{\text{on}}}{T_d R_2 C}\right) \leq \left[\frac{R_2}{R_s}\right] (1\ \text{V}) \tag{17}$$

Since the disturbing torque T_d is much smaller than the control torque T_c, which is given to be 0.14 ft-lb, and

[2]Lin, H. S., *MM '71 Derived Rate Parameter Study*, Oct. 29, 1969 (JPL internal document).

R_2C is assumed to be much larger than t_{on}, Eq. (17), to a first approximation, can be simplified to

$$R_1 \geq \frac{ET_dR_s}{T_c} = \frac{17.3 \times 15000 \times 7.37 \times 10^{-8} \times 200 \times 10^3}{0.14}$$
$$= 22.5\ \text{k}\Omega \qquad (18)$$

In summarizing the various considerations given above, we have arrived at the following conditions:

(a) $R_1 \geq 22.5\ \text{k}\Omega$

(b) $R_2 \leq 133.5\ \text{k}\Omega$

(c) $R_1 + R_2 \leq 288\ \text{k}\Omega$

(d) $19.25 \leq R_2C \leq 74.2$

(e) $R_1R_2C \leq 2164 \times 10^3$

Also, it should be recalled that most of the above results were obtained under the assumption that τ_c and τ_d are much larger than t_{on}. Thus we complement the above conditions with the inequalities:

(f) $\tau_c = \dfrac{R_1R_2C}{R_1 + R_2} >> t_{on} = 20 \times 10^{-3}$

(g) $\tau_d = R_2C >> t_{on}$

In addition to the above considerations, the convergent rate from a large initial rate or position offset toward the normal limit cycle has also been studied. For several combinations of R_1, R_2, and C that satisfied the constraints (a) to (g), computer simulations were run to examine the convergent rate. The set of values

$$R_1 = 51\ \text{k}\Omega$$
$$R_2 = 100\ \text{k}\Omega$$
$$C = 220\ \mu\text{F}$$

were finally chosen for the following reasons:

(1) They satisfy all the constraints (a) to (g).

(2) They achieve a fairly fast convergent rate (Fig. 11).

The effect of the derived rate limiter on the system performance has also been investigated. The computer results are summarized in Figs. 11 and 12. Since there are both beneficial and adverse effects resulting from the use of the derived rate limiter, it is recommended that the limiter should not be used until greater need arises for it in the future.

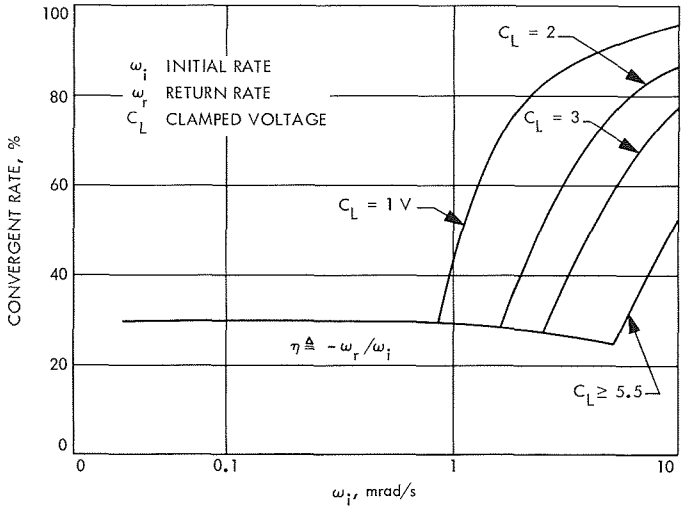

Fig. 11. Convergent rate to normal cruise mode versus initial rate

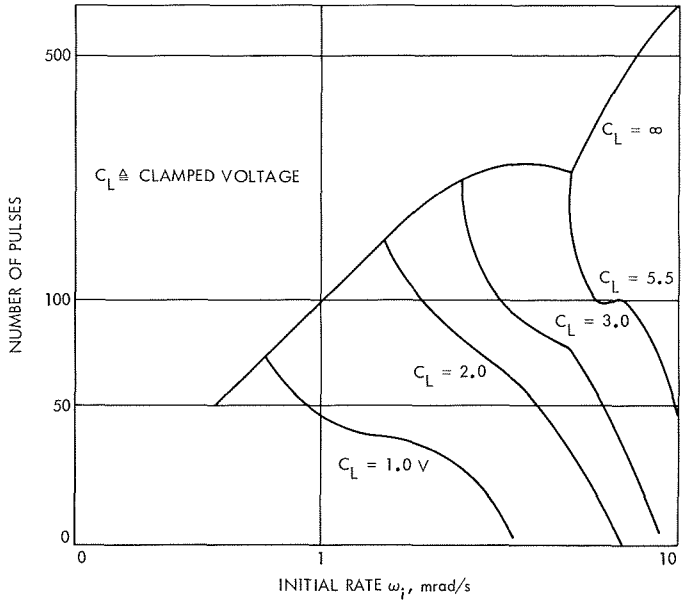

Fig. 12. Number of pulses versus initial rate

C. Engineering Mechanics

1. Introduction

During the reporting period the activities in the structure, mechanical devices, temperature control and cabling subsystems have advanced from the detail design to the fabrication phase. Engineering mechanics support has continued in the areas of mechanical systems, electronic packaging, materials and processes, structural and dynamic analysis and test, engineering documentation, and electronic parts engineering and parts analysis.

2. Mechanical Devices Subsystem: High-Gain Antenna Deployment Mechanism

The boresight of the 40-in.-dia high-gain antenna is to be permanently shifted 4.65 deg approximately twenty days after spacecraft entry into Mars orbit. The high-gain antenna deployment mechanism supports and articulates the antenna (Fig. 13). The antenna is constrained by the spacecraft configuration to lie tucked into a cavity above Bay II, bounded by the two propellant tanks, the propulsion support truss, and two solar panels folded in the launch position.

It was decided early in the design not to mount the antenna on a backing structure, as in the *Mariner* Venus '67 spacecraft, to save weight and to avoid stresses arising from differential thermal expansion between the antenna and a backing structure during flight. The mechanism was conceived to be a spring-loaded plunger, restrained by a pinpuller, acting against an antenna foot and hinged at the other two feet.

The antenna boresight movement is upward and clockwise. To reduce the movement toward the tanks, the hinge axis is located on the high side of the antenna, with the deployment mechanism foot on the low side. The two hinge points are attached to the propulsion support truss. The deployment mechanism foot is located 4.5 in. outboard of Bay II and 0.25 in. below the top of the octagon, thus requiring a strut attachment to the face of Bay II. This antenna location and motion gives a 0.62-in. static clearance to the folded solar panels and 0.30-in. clearance to the propulsion tank rings after antenna deployment.

In view of the unknown vibration environment of having two feet mounted on the truss and one foot on Bay II, and the small clearances, it was decided to isolate the antenna with three shock mounts. The 4.65-deg rotation is accommodated by tilting within each of the isolators. The isolators chosen are the Lord HT1-10 unit repackaged in a JPL-designed housing. The isolators have the additional advantage of lateral deflection to compensate for differential thermal expansion between antenna and bus and for variations in span between support points as the antenna deploys. The mechanism isolator is separated from the antenna by a spacer whose thickness is equal to one half the mechanism travel of 1.25 in. This makes the initial and final position of the isolator in line with the deployment mechanism axis with a maximum lateral movement of 0.012 in., as opposed to a shift of 0.049 in., if the spacer were not used. The vibrational response of an antenna mounted on isolators was tested, and the gain was reduced by a factor of 2 to 3. The torque on an isolator required to tilt 5 deg was measured as 6 in.-lb.

A pinpuller was chosen to restrain the antenna until deployment. The mechanism plunger is loaded against the pinpuller by a spring. Upon pinpuller firing, the spring drives the plunger to the end of its stroke and restrains the plunger in the deployed position. The spring is sized to deploy the antenna in a 1-g field. All moving interfaces are lubricated with electrofilm.

Since the deployment mechanism is rigidly mounted on Bay II, and the direction of motion of the pinpullers body in reaction to pin retraction is directed into the bay face, there was concern that the shock of the firing would disturb the electronics in Bay II. It was, therefore, decided to isolate the pinpuller shock from the bus. The pinpuller body weighs approximately 90% of the pinpuller mass. Therefore, when the pin is retracted 0.460 in. into the body, the body will want to move 0.046 in. in the opposite direction. The pinpuller is isolated by two stacks of Belleville washers that permit a motion of 0.090 in. before reaching solid height. The washers are preloaded to 120-lbf, which rises to 220 lbf at the solid height. These forces are sufficient to return the pinpuller back to its initial position after firing.

Tests will be performed in the near future to verify high-gain antenna mechanism operation. Deployment under flight conditions will be simulated in a vacuum chamber over a wide temperature range by testing with the hinge axis vertical to remove gravity effects. The pinpuller isolation will be verified by live pinpuller firings with and without the Belleville washer system installed. The deployment mechanism will be vibrationally qualified during the spacecraft type-approval (TA) and flight-acceptance (FA) tests. The antennas will be TA and FA qualified while mounted on isolators.

3. Launch Complex Equipment Cabling

The purpose of the launch complex equipment (LCE) and associated cabling is to enable the blockhouse personnel to support and monitor the spacecraft when it is mounted on the launch vehicle. This article discusses part of the LCE with emphasis on the two distribution consoles, one general-systems console, and the interconnecting cabling between all consoles. For purposes of clarification, mention is made of other LCE consoles and of certain equipment furnished by General Dynamics Corporation.

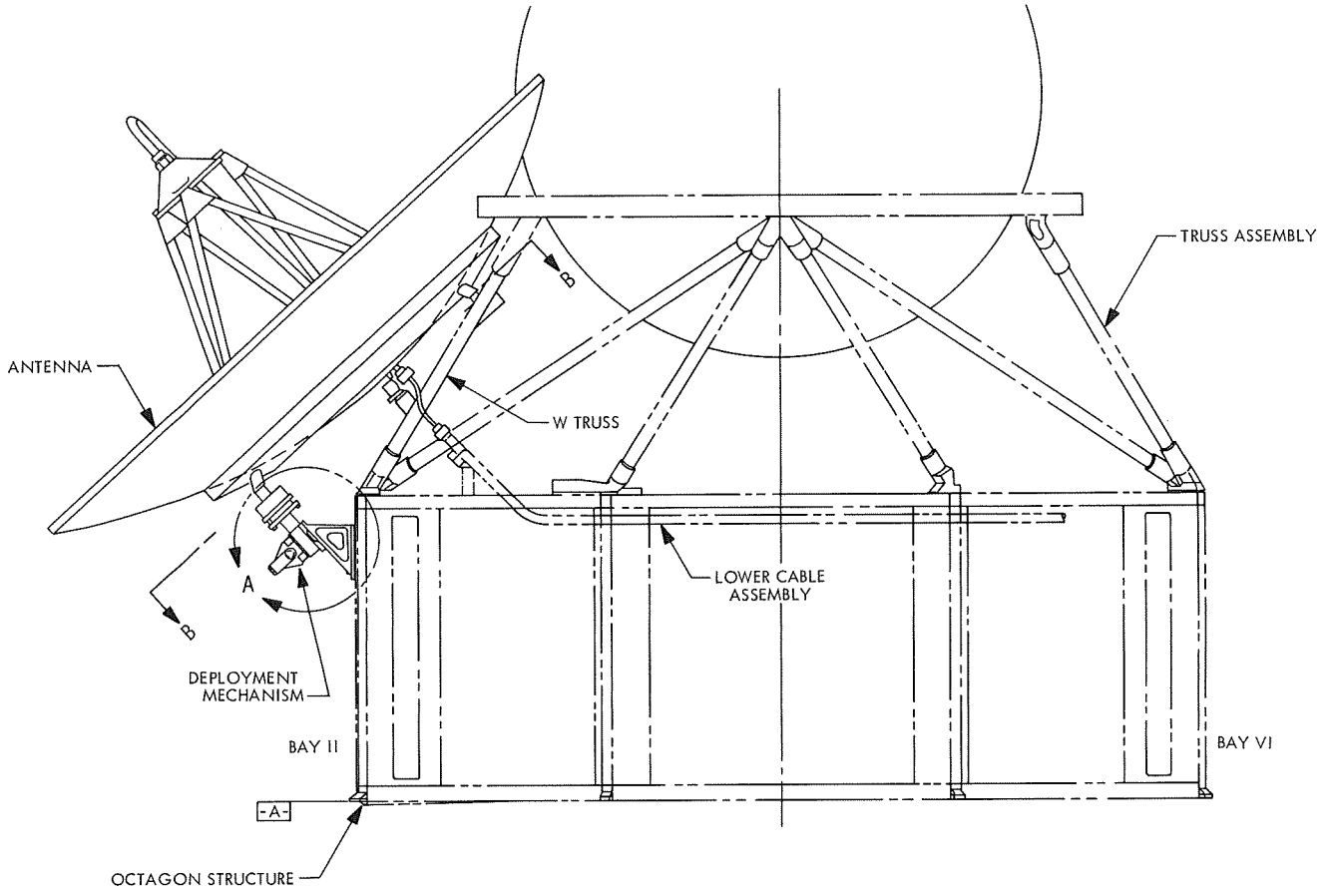

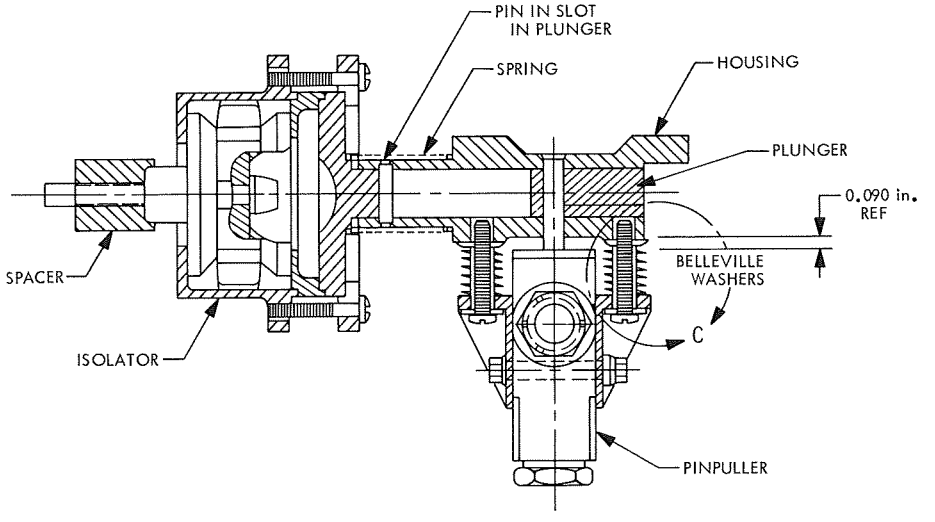

DEPLOYMENT MECHANISM

Fig. 13. *Mariner* Mars 1971 high-gain antenna deployment mechanism installation

The concept applied in the design of the *Mariner* Mars 1971 LCE was to use as much *Mariner* Mars 1969 equipment as possible. The concept arose from a careful analysis of the *Mariner* Mars 1971 design requirements and comparison with the *Mariner* Mars 1969 equipment, as well as from budget and manpower ceilings of the Project. For a description of the *Mariner* Mars 1969 LCE, refer to SPS 37-57, Vol. I, pp. 46–48.

a. Design procedure. The approach used was to first assess the number and type of wiring channels made available for the *Mariner* Mars 1971 spacecraft by deletion of equipment used on the preceding model, *Mariner* Mars 1969. Wiring required for new equipment could then be fitted into the existing channels. The *Mariner* Mars 1969 launch complex equipment was available for installation testing.

b. Typical tests using Mariner Mars 1969 LCE. The science data and bit sync signal was increased from 16.2 kHz on the *Mariner* Mars 1969 spacecraft to 132.3 kHz on the *Mariner* Mars 1971 spacecraft. It was suggested that since portions of the *Mariner* Mars 1969 circuit in the umbilical cables and vicinity was composed of twisted pair, in lieu of video pair, reflections might occur which could inadvertently trigger the system. A setup consisting of a spacecraft lower ring harness, a simulated spacecraft adapter (dummy run) harness, a simulated *Centaur* (dummy run) harness, an umbilical cable, a tower J-box and 350 ft of video pair were connected to closely approximate the cable run which would exist on *Mariner* Mars 1971 on the launch pad. A 132.3-kHz signal was sent through the system and observed on an oscilloscope. The results of this test indicated that the existing lines were satisfactory and no rework would be required on the *Mariner* Mars 1969 cabling.

At this point in the design it appears that maximum use of *Mariner* Mars 1969 LCE will be possible. Any new cables will be of conventional design.

4. Temperature Control Subsystem Hardware: Upper Thermal Blanket Development

The upper thermal blanket covers the new propulsion subsystem module. The size and configuration of the propulsion module will require a complete departure from the upper blanket design of *Mariner* Mars 1969. The upper blanket will have an area of 70 ft^2 and weigh 10 lb as compared to 19 ft^2 and 2.1 lb for *Mariner* Mars 1969.

The new blanket will incorporate meteoroid protection by the addition of a 0.007 to 0.008-in.-thick Teflon-coated glass cloth (DuPont Armalon 95049) outer layer.

The efficiency of the upper blanket is directly related to additional heater power required to keep the temperature of the propulsion subsystem within operating limits. The present goal of about 0.01 effective shield emittance corresponds to 10 W of heater power. To approach the low effective emittance requires that the blanket be constructed to avoid through seams and joints which result in thermal shorts. A similar construction was used on the *Mariner* Mars 1969 scan platform blanket, where the complex configuration could not be enclosed by a joined flat pattern construction and achieve the required efficiency.

Fabrication of a blanket without through seams and joints requires a model of the configuration to serve as a mold on which to lay up the blanket. The method used for constructing the *Mariner* Mars 1969 scan platform mold (SPS. 37-57, Vol. I, pp. 31–45), essentially encapsulating the spacecraft component with papier-mache and removing the rigid shell, is not practical for the *Mariner* Mars 1971 propulsion module mold.

The mold for the propulsion module was constructed over a mockup which contained the hardware pertinent to the blanket configuration. The mockup was then covered with aluminum screen (Fig. 14) to serve as a base for plastering. Care was taken in the screening to keep the screen below the anticipated finished plane of the mold. The first thin coat of pottery casting plaster was then applied to the screen to form a rigid shell. This configuration was very rough both in texture and in representing the finished contour. The finished planes were established by additional plaster, up to 6 in. thick, and contoured by scrapers to a smooth finish. The completed mold (Fig. 15) is very complex in shape; however, the planes were carefully developed considering the capability of the multilayer thermal blanket to conform to the configuration.

The next phase of the upper blanket development was to cover the mold with paper to determine the area and to study the handling problems of installing and removing the blanket. The paper cover (Fig. 16) was also used to determine the yardage requirements for the Armolon outer layer. This was accomplished by using paper the same width as the Armolon and using the trimmed excess wherever possible. The black lines represent the minimum seams required in the outer layer to contour to the configuration.

Fig. 14. Propulsion module temperature control blanket mockup before plastering

The mold will eventually be coated with an epoxy resin to prevent chipping and dust by surface abrasion. The finish coat will not be applied, however, until a blanket has been fabricated and the fit verified on a spacecraft.

5. Mechanical System Support: Spacecraft Hardware Utilization

In an effort to maximize hardware utilization, the configuration model spacecraft was used for the cabling mockup. Also, the same octagon structure is being used for the design test model (DTM) and the proof test model (PTM) and components for the DTM, thermal-control model (TCM), and PTM are being shared. The hardware to be shared by the DTM and TCM are the propulsion unit, thermal shield nerfing bar, low and medium-gain antenna, antenna coaxial cables, solar panel outriggers, and solar panel deployment mechanisms. A risk exists in the sharing of this hardware in that the DTM and TCM testing must occur in series, thus any slip in DTM testing is transferred directly into the TCM

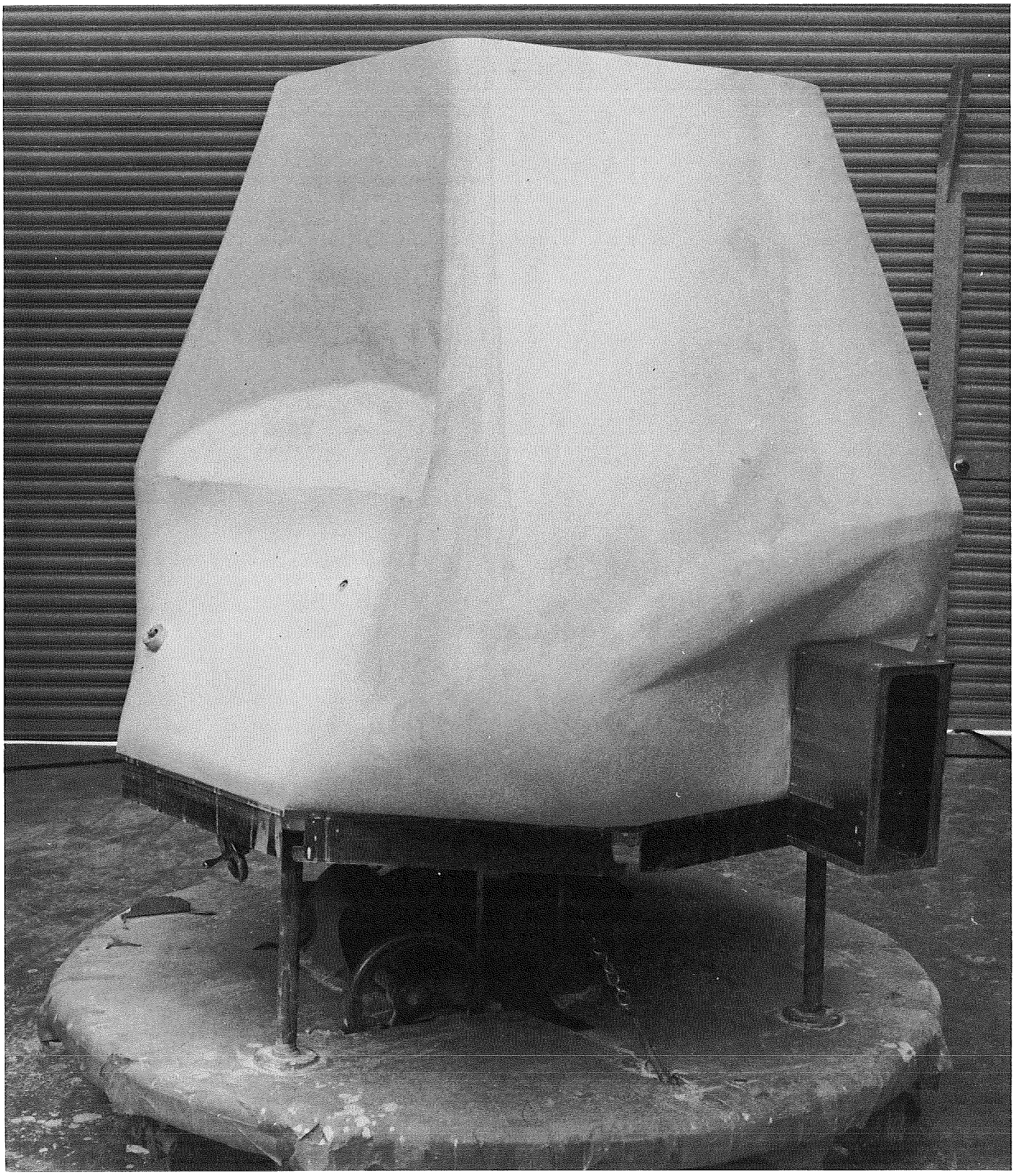

Fig. 15. Upper thermal blanket mold

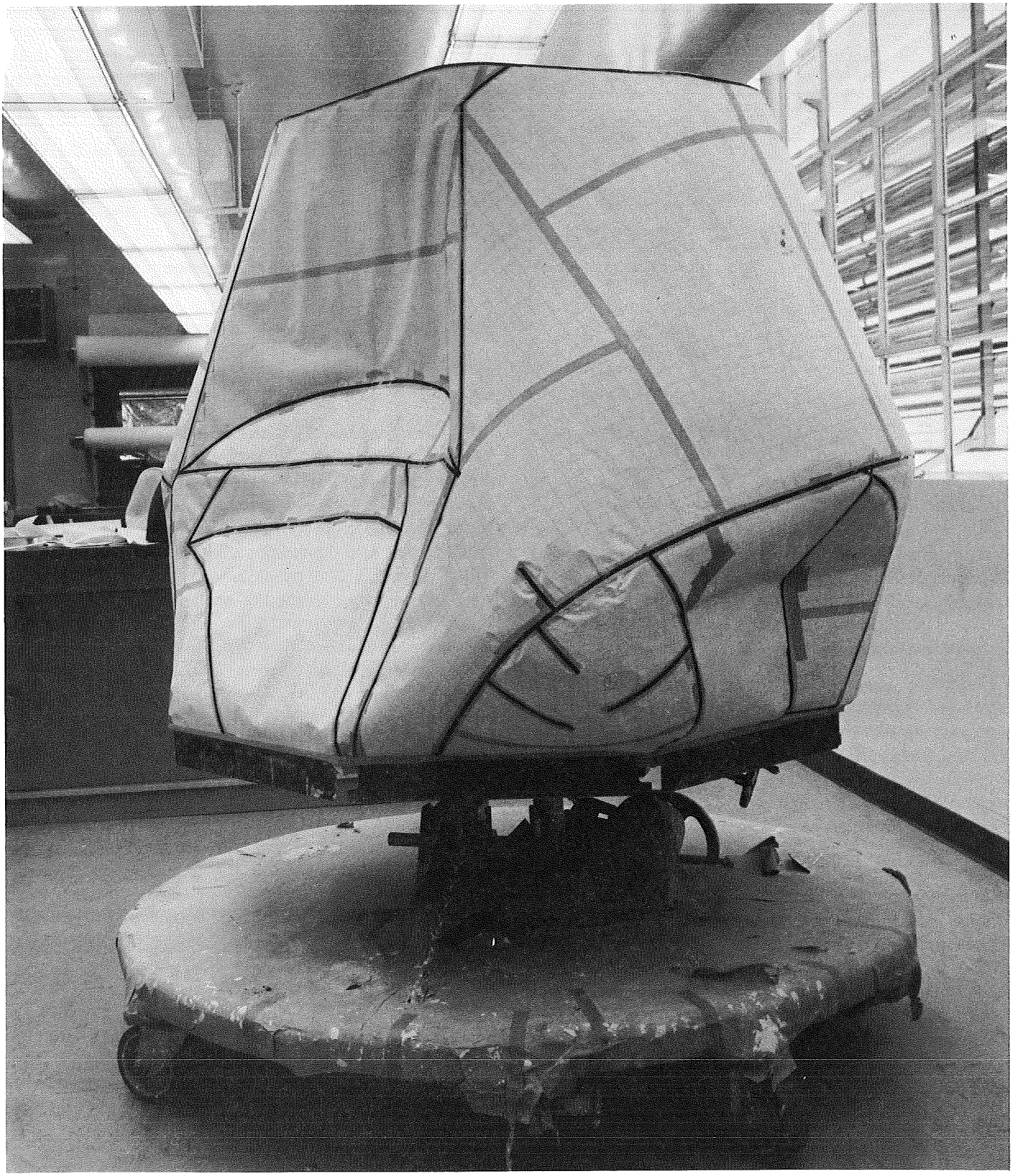

Fig. 16. Paper thermal blanket mockup on mold

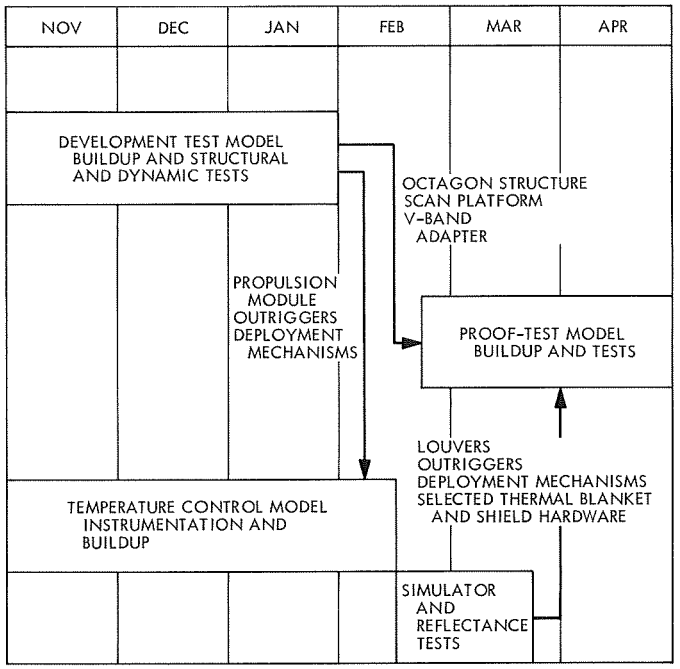

Fig. 17. DTM, TCM, PTM equipment utilization

test schedule (Fig. 17). In addition the delivery of the DTM octagon structure for use as the PTM (flight spare) is also in series with the DTM testing.

6. Electronic Packaging

Electronic assemblies form an integral part of the octagonal spacecraft structure. Subassembly structures are mechanically integrated to the spacecraft structure with the electronics protected from excessive loading by dynamic decoupling. The subassemblies have resonant frequencies above 400 Hz, while the assembly resonant frequency is designed to be above 350 Hz.

Two standard assembly designs are utilized: (1) the *Mariner* Mars 1964 configuration (Fig. 18), and (2) the *Mariner* Mars 1969 plug-in subassembly configuration shown in Fig. 19. Within an assembly, the subassembly profile is standardized to facilitate location flexibility. To optimize design and to reduce interconnections, two profile standards are utilized in the *Mariner* Mars 1969 configuration shown in Fig. 19, and subassembly width is varied to comply with equipment design requirements and packaging techniques.

The *Mariner* Mars 1971 spacecraft uses the *Mariner* Mars 1969 spacecraft configuration as a baseline. The spacecraft electronics are housed around the periphery of the octagonal supporting structure which is 18 in. high and 54 in. across the diagonal. The spacecraft structure contains eight removable and replaceable electronic assemblies. In the *Mariner* Mars 1969 spacecraft there were only seven electronic assemblies because the propulsion subsystem was mounted in Bay II.

The following gross changes were made in the electronic packaging layout:

(1) The Bay VIII (power regulator assembly) was moved to Bay I.

(2) The Bay I (power conversion) was moved to Bay II.

(3) The Ni–Cd battery was mounted in Bay VIII.

(4) The pyro switching assembly (PSA) was mounted on the top of the bus.

On *Mariner* Mars 1969, the PSA was made redundant by fabricating and installing two identical subassemblies on the spacecraft. In order to make the elements act redundantly, it required a special harness and an extra bracket on the spacecraft. This not only added weight, made mating and demating of the connectors an extreme problem, but it also presented complexity to the PSA checkout at Cape Kennedy's explosive safe area. A redundant PSA for *Mariner* Mars 1971 was designed into one subassembly and was to be installed into Bay II. After reviewing the spacecraft configuration, it was found that the PSA could be mounted on the octagon upper ring between Bays IV and V. This position helped to alleviate the foregoing problems.

7. Temperature Control Design: TCM Test Planning

The *Mariner* Mars 1971 TCM testing is presently scheduled to begin in mid-February of 1970. The following test objectives are felt to be of primary importance:

(1) Verify that the overall thermal design is adequate.

(2) Empirically determine the thermal characteristics of the design.

(3) Obtain data on particular modes which cannot be tested with a flight spacecraft.

(4) Obtain good vacuum data on the effects of post-engine firing thermal soak-back.

The thermal design is considered adequate when it can maintain spacecraft temperatures within acceptable limits for all possible mission modes. Hopefully, this adequacy can be verified at the outset of the TCM test

by choosing two modes that can bracket all mission thermal environments.

Types of tests which are candidates for incorporation into the TCM test plan are listed below:

(1) Solar sensitivity.

(2) Power sensitivity.

(3) Determination of the thermal coupling between selected spacecraft components.

(4) Sensitivity of the spacecraft to thermal design changes.

(5) Transients.

(6) Finding correlation between TCM and flight spacecraft simulator test results.

(7) Verification of the feasibility of PTM and flight spacecraft simulator test techniques.

(8) Spacecraft's response to a ground testing environment (i.e., in air).

The TCM is a full-scale spacecraft that is flightlike in geometrical configuration, but houses no flightlike electronics, their power dissipation being provided by resistance heaters. The weight of the TCM is intentionally minimized to achieve a low thermal time constant, but all significant thermal paths, both radiative and conductive, are accurately duplicated or simulated.

The 25-ft space simulator with an 8-ft-dia sun will be used for the TCM test. It is anticipated that approximately 350 thermocouples and 60 Variac-controlled ac heaters will be required. The integrated data-acquisition and control (IDAC) system will be used for data acquisition.

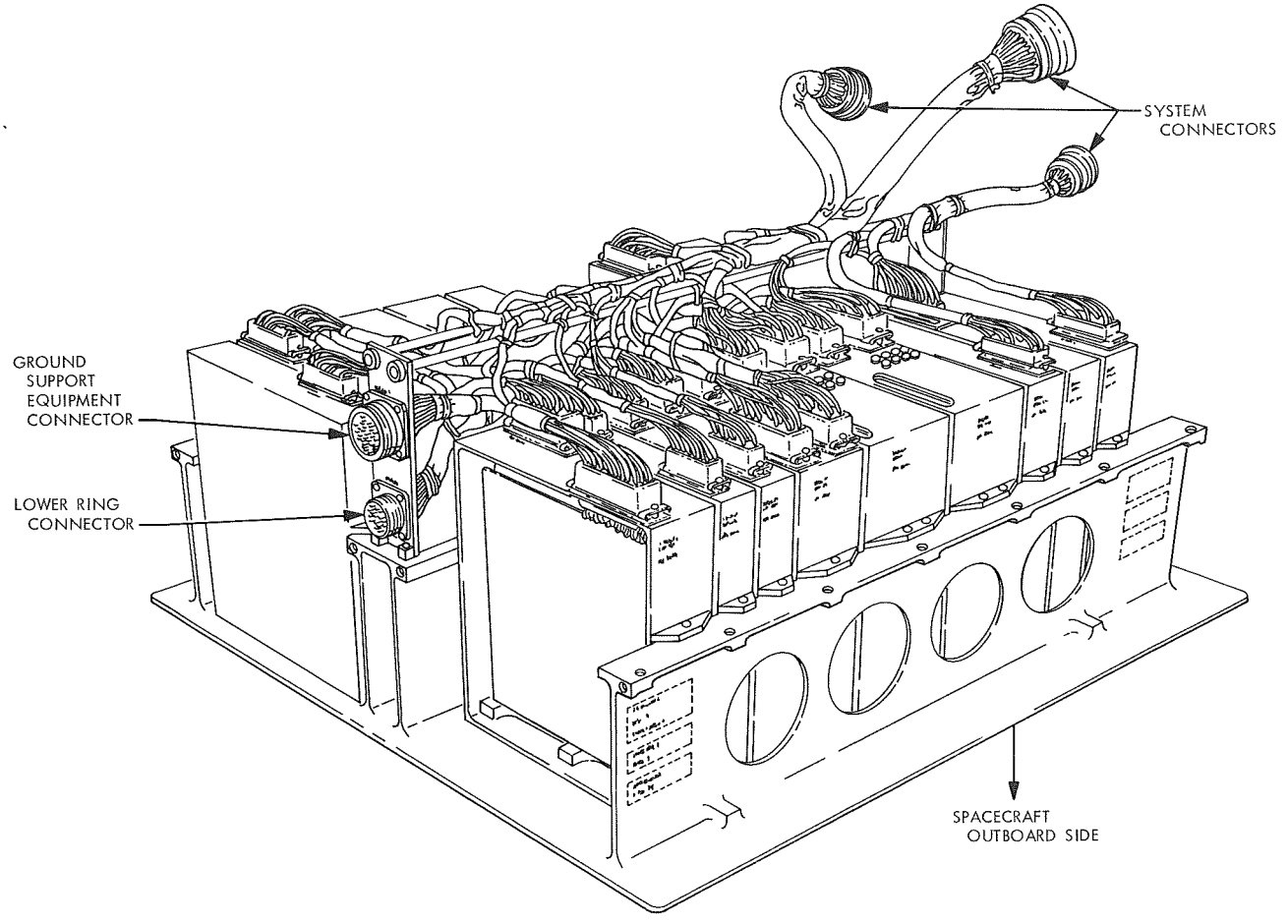

Fig. 18. Typical *Mariner* Mars 1964 electronic assembly used in *Mariner* Mars 1971 spacecraft

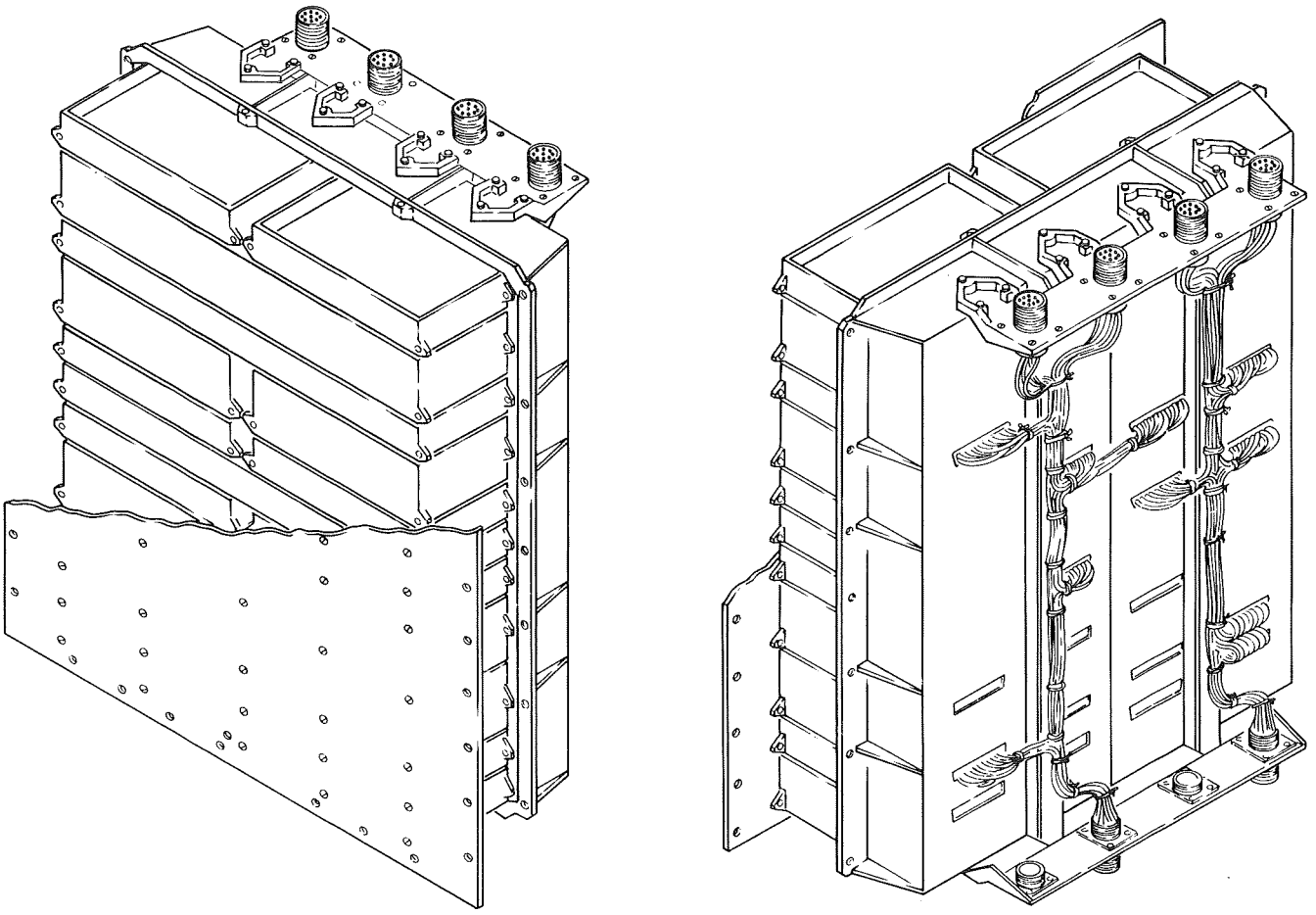

Fig. 19. Typical *Mariner* Mars 1969 plug-in electronic subassembly

8. Structures and Dynamics Analysis and Tests: Fracture Mechanics of Propellant Tank Design

a. Introduction. The design of the propellant tanks was the result of a team effort that involved the talents of specialists in the areas of propulsion, structures, materials, and manufacturing. The basic considerations that influenced the design configuration the most were:

(1) The propellants to be stored.

(2) Propellant volumes.

(3) Pressurization, operational requirements.

(4) Design loading conditions.

(5) Operating temperatures.

(6) Adaptation of the tank supports to existing *Mariner* octagon structure.

Twin spherical tanks of 6Al-4V titanium alloy were selected for the basic design based on the preliminary design considerations. Several materials were screened for tank applications, including 2219 aluminum alloy. However, the titanium alloy was chosen because of its well-known structural efficiency as well as its satisfactory performance at JPL. Other configurations studied for the final design were:

(1) Four off-the-shelf tanks of smaller diameter procured from existing or phased-out Air Force programs.

(2) Twin oblate tanks stacked one on top of the other.

(3) Twin cylindrical tanks arranged in tandem.

The twin oblate or cylindrical tank configuration would have raised the CG of the propellant mass to unacceptable levels, i.e., overturning moment was *the* prime constraint in being able to use existing octagon structures and adapters with little or no modification. The four tank configuration of off-the-shelf hardware caused complex plumbing problems and possible propellant CG

migrations that could impair the reliability of the mission. Besides being the most structurally efficient, the twin spherical tanks had a CG that was within acceptable limits and simplified plumbing requirements.

b. Design criteria. The propulsion subsystem requires long-term pressurized storage ($\geq$1000 h) of two stress-corrosive fluids—nitrogen tetroxide (N_2O_4) and monomethyl hydrazine (MMH). Experience with the *Lunar Orbiter* and *Apollo* programs had shown that 6Al-4V titanium alloy was the most efficient material for the pressurized storage of these propellants. A heat-treat level of 150 ksi minimum yield strength was selected for the tank material. Favorable experiences with 28-in.-dia *Applications Technology Satellite* motor cases and enhanced ductility as compared to 160 ksi minimum yield strength were the main reasons for selecting this heat-treat level. However, only limited data existed for this alloy's crack propagation properties in contact with these propellants; that data was applicable only to the *Apollo* tank material which had a heat-treat level of 160 ksi.

The fracture mechanics design approach for determination of the allowable stress levels for this alloy in contact with corrosive fluids was based upon the following basic equation:

$$\sigma_{op} = \sigma_{pr}\left(\frac{K_{th(op)}}{K_{Ic(pr)}}\right) \quad (1)$$

where

$K_{th(op)}$ = crack propagation threshold stress intensity in the corrosive environment (i.e., the stress intensity at which *no* crack growth will occur in the tank in its operating environment), ksi (in.$^{1/2}$)

$K_{Ic(pr)}$ = fracture toughness of the material in the proof-test environment (liquid nitrogen), ksi (in.$^{1/2}$)

σ_{pr} = maximum proof stress, ksi

σ_{op} = maximum allowable stress at which the largest existing crack in the material will not propagate in the stress-corrosive environment, ksi.

A maximum operating stress of 90 ksi was selected for the propellant tanks. This value was derived using Eq. (1) and a downgraded approximation of the *Apollo* fracture toughness data. Application of a factor of safety on this data of 1.25[3] resulted in a maximum allowable stress of 72 ksi for those areas of the propellant tanks exposed to N_2O_4 and MMH for long periods of time.

The proof-test environment for the propellant tanks—liquid nitrogen at −320°F—was chosen for three distinct benefits:

(1) The strength of Ti6Al-4V is significantly increased at −320°F over its room temperature allowable strength. Therefore, σ_{pr} can also be significantly greater.

(2) The reduced ductility of this alloy at LN_2 temperatures limits the residual stresses that *could* exist in the tank due to welding, etc. In other words, undetected residual stresses of a serious nature could cause failure of the tank during the LN_2 proof test.

(3) The fracture toughness of Ti-6Al-4V is substantially lowered at −320°F which permits the detection or screening of smaller flaws in the tank. Clarification of the advantage of using a liquid-nitrogen proof test can best be demonstrated by referring to Fig. 20.

Because of the decreased fracture toughness of this particular alloy in LN_2, failure will occur at a flaw size (a_{pr}) smaller than the flaw that would cause growth in

[3]*Mariner Mars 1971 Structural Design Criteria* requires that a minimum factor of safety of 1.25 shall be used on all structures.

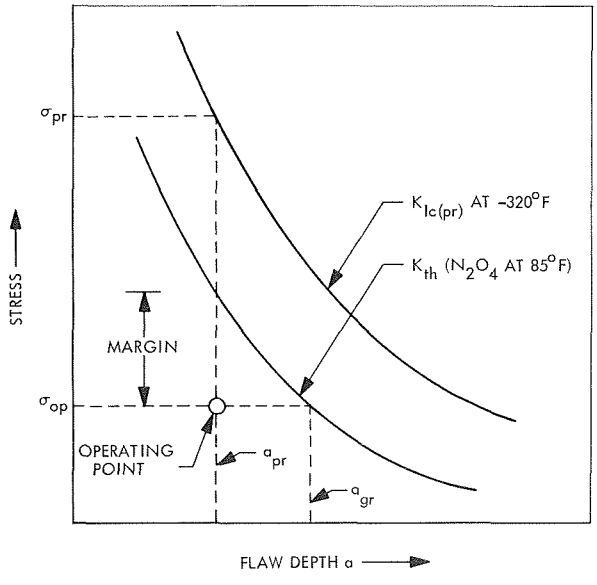

Fig. 20. Fracture toughness $K_{Ic(pr)}$ and threshold stress intensity K_{th} as a function of flaw size

the operating environment of N_2O_4 (a_{gr}). Since the limiting value of K_{th} has been established by test, it is only necessary to "back off" to an operating point established by a_{pr}. The LN_2 proof test will have demonstrated that no defect of this size (or greater) can exist in the tank under a static stress condition. A margin of operation can then be established by noting the stress at the point where a_{pr} intersects the K_{th} curve, i.e., where the flaw size a_{pr} would become unstable and start to grow.

c. Tank design. The tanks were fabricated from forged hemispheres of 6Al-4V titanium alloy in the solution treated and aged condition. This process yielded basic material tensile properties of 150 ksi yield strength and 160 ksi ultimate strength. The two dome forgings were initially rough-machined and then solution-treated and stress-relieved (partial aging). The domes were then finish-machined to their design thickness and fusion welded together by the tungsten inert gas process. Vacuum aging after welding was used to develop full mechanical properties.

The significant features of the propellant tank design are shown in Fig. 21. Due to the requirements of the Teflon bladder, the tank neck could not be machined symmetrically, i.e., with an equal portion of the bolting flange protruding in the tank. As a result, the reinforcement of the neck area of the tank was about 30% heavier than if a symmetrical flange had been used. The local thickness of the membrane adjacent to the bolting flange was 0.100 in., tapering to a basic membrane thickness of 0.033 in. The discontinuity stresses arising from the bolting flange and the standpipe closure assembly were carefully considered in deriving the optimum tank flange and reinforcement. In addition, sufficient margin was maintained to account for external loading into the tank neck due to thermal gradients, rocket engine inertia and firing, or other significant loading conditions revealed by the spacecraft composite analysis.

Serrations were provided on the tank and standpipe flanges to "bite" into a soft aluminum crush gasket. Thirty-two 0.25-in. bolts were torqued to maintain a compression force on the gasket well in excess of that required to assure a reliable seal. Welding the end closure shut to provide the ultimate seal was considered but discarded, due to the desire for reentry into the tank to repair the bladder, etc.

Each tank was mounted to the propulsion support structure by four symmetrically located tabs, as shown in Fig. 21. The tabs were designed with sufficient length to minimize bending stress into the tank due to radial loads. At the same time, the tabs had to be of sufficient section to preclude buckling due to axial compressive loads coupled with possible eccentricities during bolt-up.

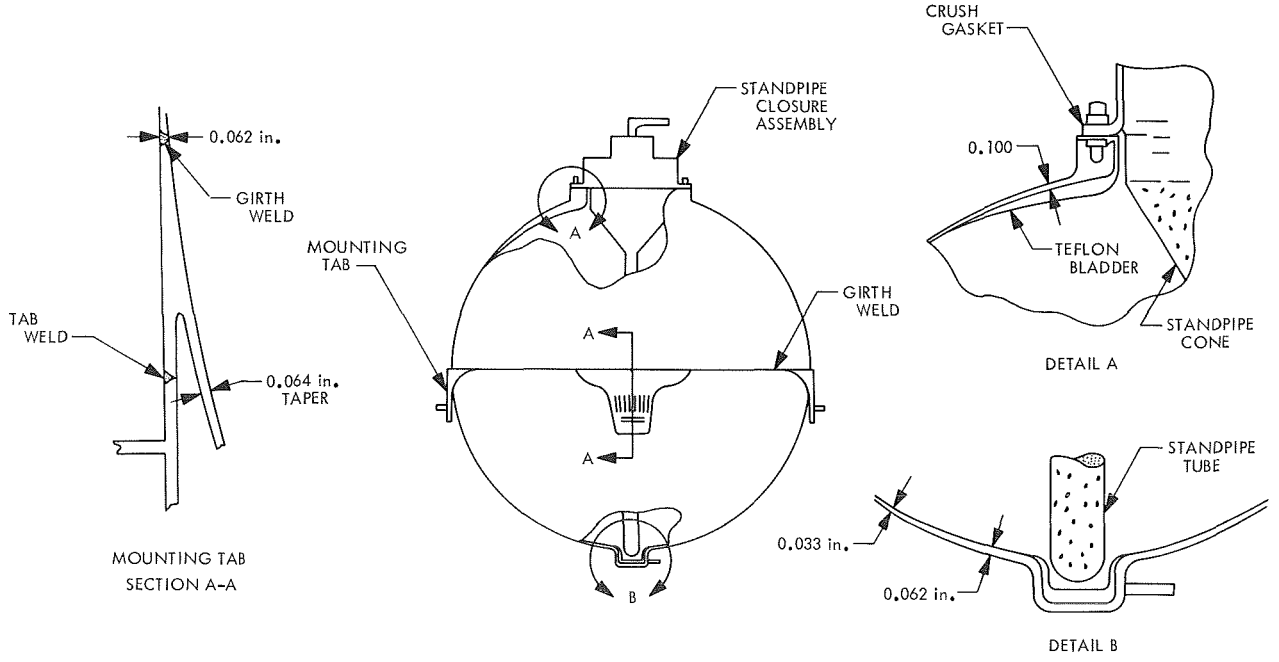

Fig. 21. Propellant tank fabrication

The areas of the tank where the tab was located were handled with particular care. The maximum discontinuity bending stresses were introduced into the tank at section A–A as well as the inertia loads due to flight. This configuration, which made no attempt to minimize discontinuity stresses, was chosen because of its fabricability and "cleanliness," i.e., the pressure-carrying transition area of the tank could be readily machined and would not be disturbed by any structural attachment welds of the tabs. The tank girth weld was located a suitable distance above the attachment area to minimize the effect of the discontinuity area on the weld stress.

d. Material test program. As stated, no values of K_{th} and $K_{Ic(pr)}$ existed for the tank material strength condition, and the *Apollo* data was not considered to be conclusive. Therefore, a test program was awarded to the Boeing Company[4] to measure these values on forgings from two different heats of 6Al-4V titanium alloy left over from the *Surveyor* program and heat-treated to *Mariner* Mars 1971 strength levels. Tests were conducted on the basic forging stock, weld metal, and heat-affected zones (HAZ). Surface flawed specimens of similar thickness as the tank section being investigated were used for all tests. The forging stock specimens which represented the basic tank membrane were 0.033 in. thick. The weld and HAZ specimens were 0.055-in. thick, reflecting the dimensions of the girth weld area of the tank. The specimen configuration and crack geometry are shown in Fig. 22.

The initial crack depth was approximately one-half the specimen thickness t. Crack length was five times crack depth and specimen width about ten times crack length. K_{th} was measured in N_2O_4 procured to Manned Spacecraft Center specifications. The specimens were statically loaded and exposed to N_2O_4 for 1000 h. All determinations of K_{th} were made at a temperature of approximately 85°F. The initial nitrous oxide (NO) content of the N_2O_4 was 0.64%. Since the propellant tanks were to be proof-tested to a stress level of 200,000 lb/in.^{2} in liquid nitrogen (−320°F), the values of $K_{Ic(pr)}$ were measured in LN_2. The complete results of this test program are reported here as obtained from the Boeing Company.[5] These results are summarized in Table 2.

[4]Aerospace Group, Seattle, Wash.

[5]Masters, J. N., Haese, W. P., and Bixler, W. D., "Fracture and Nitrogen Tetroxide/Sustained Load Flaw Growth of 6Al-4V Titanium," October, 1969 (JPL internal document).

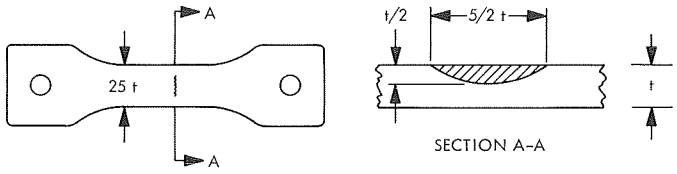

Fig. 22. Fracture mechanics tensile specimen

The propellant tanks were designed to satisfy the criteria shown in Tables 3, 4, and 5. The design adequacy of the propellant tank under static pressure was demonstrated with the first tank built. The room temperature "sizing" test at 600 psig and the LN_2 proof test at 840 psig disclosed no measurable bulging or indications of yielding. Some apprehension was expressed due to an abnormal amount of weld mismatch in one area of the girth weld. However, the hydrostatic sizing operation apparently yielded out the effects of this discontinuity.

e. Design margins. Due to the plasticity effects noted in Table 2 for heat G-804, the data analysis efforts were concentrated on heat 301275. Examination of the data disclosed that the limiting value of stress intensity factor K_{th} occurred in the forged coupons representing the basic membrane of the tank. This limiting value of K_{th}

Table 2. Summary of fracture mechanics test program for propellant tanks

Heat No.	Material condition	K_{th} of N_2O_4 for 1000 h at 85°F, ksi (in.$^{1/2}$)	$K_{Ic(pr)}$ at −320°F, ksi (in.$^{1/2}$)	F_{ty} (avg) at 85°F, ksi	F_{tu} (avg) at 85°F, ksi
G-804	Forged	30.02	53.83[b]		
	Forged	29.50	58.76[b]		
	Forged	—	54.83[b]	153.0	173.0
	Weld	31.77	45.96		
	Weld	29.14	—	133.3	153.6
	HAZ[a]	31.61	42.17		
301275	Forged	27.78	44.53		
	Forged	27.46	46.61		
	Forged	—	48.02	156.0	174.5
	Weld	30.97	37.45		
	Weld	30.68	40.07	137.9	155.9
	HAZ	29.14	32.14	—	—
	HAZ	28.73	—		

[a]HAZ = heat-affected zone.
[b]This data believed invalid due to excessive plasticity effects.

Table 3. Pressurization requirements for propellant tanks

Condition	Pressure, psig	Comment
Fill	0 (vacuum)	Tanks evacuated for filling
Pad	100.0	For personnel safety
Boost (launch)	100.0	Added to inertia forces
Operation (nominal)	268.0	Long-term requirement
Operation (max)	300.0	Temperature ≈105°F
System proof leak check	450.0	No personnel exposure Inert fluids
Sizing	600.0	Room temperature
Proof	840.0	LN_2 temperature (−320°F)

Table 4. Allowable stresses for propellant tanks

Condition	Welds, ksi	Base material, ksi	Comment
Vacuum	—	−3.5	Collapse stability based on 0.033-in. membrane
Boost	63.0	90.0	Ultimate used for short-term transient condition
Operation (max)	50.0	72.0	Long-term propellant storage requirement
System proof	76.0	108.0	No personnel exposure Inert fluids
Sizing	99.0	142.0	Room temperature
Proof	139.0	200.0	−320°F

at which *no* growth was observed to occur was 27.78 ksi (in.$^{1/2}$).

The fracture toughness properties for heat 301275 in LN_2 were assumed to be normally distributed. These values were statistically reduced[6] to yield a limiting value of $K_{Ic(pr)}$ that would *not* be exceeded by more than 10% of the expected population with 95% confidence. In other words, the confidence is 95% that 90 out of 100 specimens with cracks of the configuration tested in LN_2 would not yield a fracture toughness value higher than 57.23 ksi (in.$^{1/2}$).

[6]Schumacher, J., *Statistical Determination of Strength Properties*, Convair Report No. AZS-27-274A, 1958.

Table 5. Inertia requirements for propellant tanks (static equivalents)

Condition	Acceleration, g		Comment
	Axial	Lateral	
Boost	−12.0 + 4.0	0.0	− (Thrust) + (Uplift)
Boost	0.0	4.0	Any direction

Table 6. Summary of estimated factors of safety for propellant tanks under static pressure

Temperature, °F	Pressure, psig	Factor of safety for membrane	Factor of safety for weld	Comment
85	100.0	4.1	4.9	Pad pressure
	272.0	1.50	1.8	Maximum man-rated pressure
	300.0	1.36	1.63	Maximum expected operation pressure
	326.0	1.25	1.50	Maximum allowable operation pressure
105	100.0	3.70	4.45	Pad pressure
	248.0	1.50	1.97	Maximum man-rated pressure
	296.0	1.25	1.65	Maximum allowable operation pressure

If the original fracture mechanics equation is rearranged and written in terms of tank pressure and factor of safety, the following results are obtained:

$$\text{Factor of safety (FS)} = \frac{P_{pr}}{P_{op}}\left[\frac{K_{th}}{K_{Ic(pr)}}\right]$$

$$= \frac{840 \text{ psig}}{300 \text{ psig}}\left[\frac{27.78 \text{ ksi (in.}^{1/2})}{57.23 \text{ ksi (in.}^{1/2})}\right]$$

$$= 1.36$$

Thus, the factor of safety for the basic tank membrane under a static pressure of 300 psig in the presence of N_2O_4 at 85°F is 1.36. This result verifies the assumptions used in establishing the original design stress based on the downgraded *Apollo* data. Table 6 lists a summary of the FS estimates of the propellant tanks under various conditions of static pressure.

Table 7. Results of tests of bonding materials

Adhesive	Materials		Ultimate tensile load, lb	0.2% offset yield load, lb	Failure location	Cure cycle
	Fitting	Tube				
Epon 913	Al	Be	5900	4920	Adhesive joint	Bonded 18 h after etching, room temperature cure 24 h, oven cure 4 h at 125°F
Epon 913	Mg	Be	5580	4800	Adhesive joint	Bonded 18 h after etching, room temperature cure 4 days, oven cure 4 h at 125°F
Epon 913	Mg	Be	4200		Adhesive joint	
Epon 913	Mg	Be	5900	4800	Be tube	
Epon 913	Mg	Be	5760	4700	Adhesive joint	
EC 2216	Al	Be	3510		Adhesive joint	
Epon 913	Al	Al	3360		Adhesive joint	Bonded 18 h after etching, room temperature cure 7 days, cure 4 h at 125°F

9. Materials

Three areas of materials and processes support to the Project are discussed:

a. Adhesive bonding, beryllium propulsion support truss. The results of the tests described in SPS 37-58 Vol. I, pp. 56–59, to obtain test information on the bonding of combinations of materials and surface preparations of beryllium and aluminum tubing to similar combinations of dumbbell fittings (Fig. 23) which would be tension tested to failure are given in Table 7.

As can be seen from the above data, the combination of lighter weight magnesium (Dow 17 coated) with beryllium tubing gave ultimate loads of 5000 to 5900 lb using the selected Epon 913 adhesive. The maximum expected flight loading is 2000 lb, 3-sigma maximum.

b. Solar panel adhesive bonding. T-peel strengths of 8 lb/in. (min) of the combination of 0.005-in.-thick 5052 H-19 foil to 5052 H-19 bonded with Epon 913 adhesive have been developed for the *Mariner* Mars 1971 solar panels. The previous efforts achieved ½ to 5.6 lb/in. T-peel strength. A laboratory simulated production cleaning-bonding cycle was initiated first in order to analyze the influence of processing variables. Some of these included:

(1) Method of precleaning the sheet (if necessary) by vapor degreasing versus various solvent wipings.

(2) Concentration, time, and temperature in alkaline soaking solution.

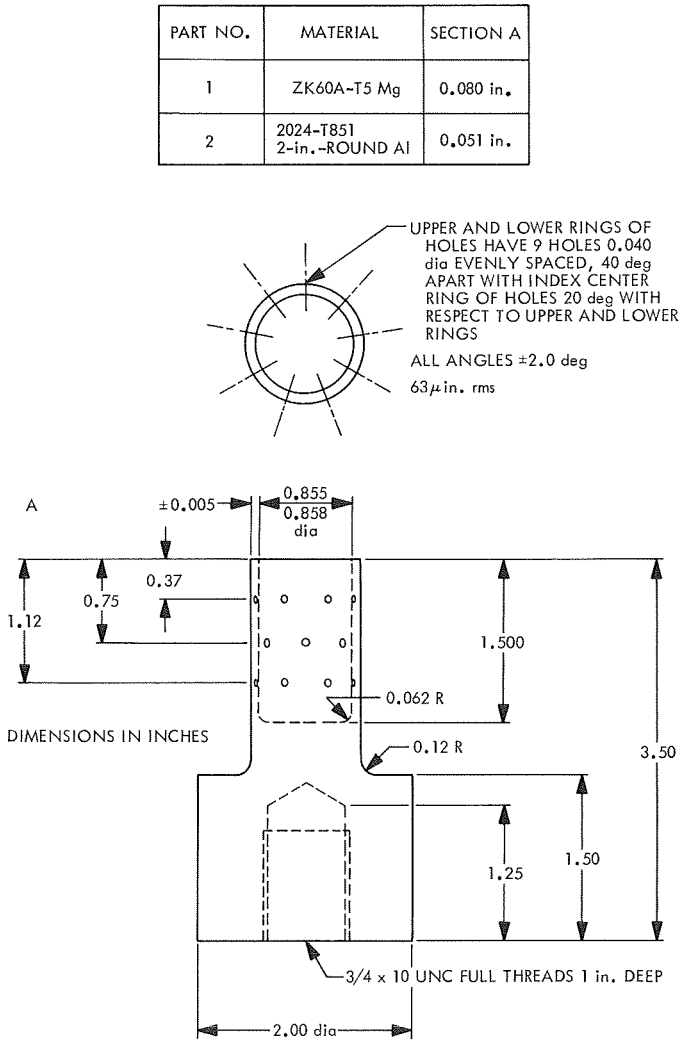

Fig. 23. Dumbbell fitting for beryllium and aluminum bonding tests

(3) Time, temperature, and pH of tap water rinsing.

(4) Time and temperature of deionizing water rinse.

(5) Concentration, temperature, aging time, and immersion time of 5052 H-19 sheet in a solution of chromic acid. sulfuric acid, and distilled water.

(6) Water-rinsing conditions and oven-drying time and temperature.

A successful laboratory cleaning-bonding cycle was established and performed in the contractor's production facility. The laboratory cleaning-bonding cycle established T-peel strengths between 9 and 12 lb/in. and was duplicated at the contractor's facility.

The successful cleaning-bonding cycle consisted of the following:

(1) Immersion in alkaline solution (Ridolene No. 53) for 15 ± 1 min at 160 ± 5°F at a concentration of 4 oz per gallon of solution.

(2) Room temperature tap water rinse 30 to 60 s, pH of 3.5 to 7.5.

(3) Room temperature deionized water rinse for 2 to 2.5 min.

(4) Immersion in acid solution, 38.5 to 41.5 oz per gallon of sulfuric acid, 4.0 to 4.8 oz per gallon of sodium dichromate, and the balance water, at 150 to 160°F for 15 ± 1 min.

(5) Room temperature tap water rinse 30 to 60 s, pH of 3.5 to 7.5.

(6) Room temperature deionized water rinse for 2 to 2.5 min.

(7) Oven dry at 130 ± 10°F for 15 ± 1 min.

(8) Apply adhesive within 6 h after cleaning and cure adhesive for 3 to 3.25 h at 180 ± 5°F.

c. Television subsystem alternate shutter blade material study. The TV camera B shutter is constructed of 0.003-in.-thick aluminum type 1100-H24 formed with corrugation as shown in Fig. 24 and black anodized on the under side. The pointing of this camera to the sun unintentionally during maneuvers would result in blade temperatures up to 675°F, producing excessive distortion. A study was conducted to find a suitable alternate material for this application which would: (1) have structural stability to 700°F, (2) good thermal conductivity, (3) modulus of elasticity higher than aluminum,

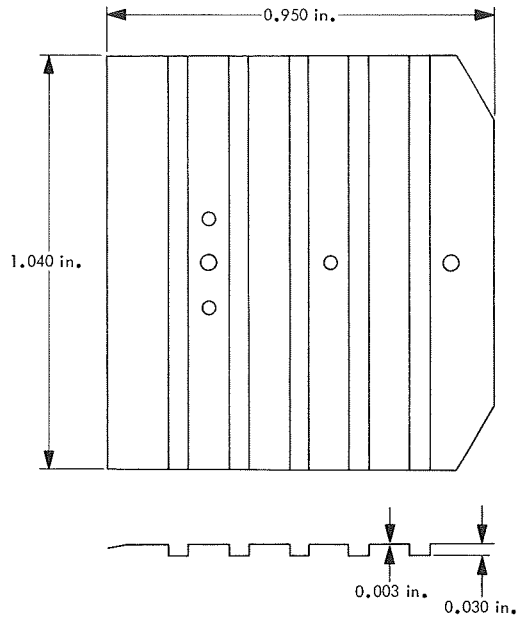

Fig. 24. *Mariner* Mars 1971 TV subsystem shutter blade configuration

(4) no increase in weight, and (5) ability to be coated for thermal control.

The most attractive alternate material for consideration in this application was found to be beryllium foil. The following attributes of beryllium led to this conclusion:

(1) Beryllium is approximately 30% lighter than aluminum—foil 4.4 mils thick would weigh no more than 3 mils of aluminum. Therefore, a potential to decrease shutter blade weight exists.

(2) No phase changes occur to temperatures in excess of 800°F.

(3) Yield strength of 32,000 psi at 800°F.

(4) Modulus of elasticity of approximately 42,000,000 psi—over four times that of aluminum.

(5) Thermal conductivity is comparable to aluminum but specific heat is two times that of aluminum, indicating less temperature rise per unit time of exposure to solar heating.

(6) Existing anodizing methods result in good "black" coating; vapor-deposited silver with SiO overcoat may be best coating for solar reflectance.

(7) Coefficient of thermal expansion is half that of aluminum, which tends to minimize distortion due to temperature variations.

(8) Beryllium foil is readily available from two sources in thickness down to 1 mil.

A test program was initiated to evaluate beryllium foil disks coated with thermal-control materials. Disks of high-purity beryllium 1-in. dia × 0.004-in. thick were procured for the following study:

Anodized samples. A black anodized coating was applied to one side of two disks each in normal, thin, and thick anodized coating. The coatings were evaluated by determination of ϵ_N values, which were 0.4 to 0.55 for the thin anodize versus 0.72 to 0.75 for the normal and thick types. It was concluded that normal anodize coating thickness was appropriate for this application.

Silver–silicon monoxide (Ag–SiO) coated samples. A typical vacuum-deposition mirror process for application of a silver layer with SiO overcoating was applied to two foil coupons. The value of solar reflectance α_s was determined to be in the range 0.12 to 0.14 and total normal emittance ϵ_N = 0.04. Adhesion was satisfactory.

Thermal analysis indicated that maximum temperature would be 430°F with the thermal-control coatings applied to beryllium foil. The foil should be capable of heating to this temperature without significant distortion if properly configured. Studies of an actual design and fabrication methods for same would be the next logical step. Chemical milling of thicker foil, or hot-forming corrugations would be promising methods for producing stiffening, if required.

Further effort to qualify beryllium for this application has been halted, since *Mariner* Mars 1969 experience has proved that the avoidance of sun view can be achieved.

III. *Viking* Project, Orbiter System and Project Support

PLANETARY—INTERPLANETARY PROGRAM

A. Project Description and Status

The primary objective of the *Viking* Project is to send two vehicles to the planet Mars to perform scientific experiments directed toward enhancing current knowledge about the physical characteristics of the planet, particularly its capability for supporting life and possible evidence of life. The two vehicles, each consisting of an orbiter system and a lander system, are anticipated for launch during 1973. The orbiter system will be developed by JPL, and the lander system will be developed by the Martin-Marietta Corp. Langley Research Center has overall management responsibility for the *Viking* Project.

The orbiter system will transport and inject the lander system at the appropriate point for a selected landing site and will relay telemetered data from the lander to earth. Scientific instruments on the orbiter will be used to measure atmospheric and surface parameters at various times and locations to determine the dynamic characteristics of the planet. The topography of Mars will be mapped during orbital operations, with special emphasis on mapping the proposed landing site prior to deorbit of the lander system. Both visual and infrared coverage will be possible during the presently planned 90 days of orbital operations.

During entry and after landing, the scientific instruments on the lander will measure Mars' atmospheric composition, temperature, pressure, and density. After landing, the topography of the landing site will be mapped, and measurements will be made of the planet's surface composition, temperature, pressure, humidity, and wind speed. Of particular interest in the surface measurements are the type of organic compounds present, if any, and the amount and form of water. A gas chromatograph/mass spectrometer, for measuring both atmospheric and surface composition, is being developed by JPL. The surface soil analyses will be directed at detecting evidence of growth and/or metabolism.

B. Guidance and Control

1. Radiation Characteristics of *Viking* 675 W(th) Intact Reentry Heat Sources

a. Introduction. Of major importance to the *Viking* orbiter program is the extent of interference, if any, of gamma and neutron radiation from the radioisotope thermoelectric generators (RTG's) aboard the lander upon subsystems of the orbiter. Such interference might be either transient, as in the case of spurious signals from science instruments or semiconductor electronics, or more permanent, such as glass darkening or breakdown of organic lubricants. All such effects are dependent upon the type of radiation (i.e., γ or n), its spectral energy distribution, and either the dose rates or accumulated dose levels. Each of these is, in turn, dependent upon spatial position relative to the RTG, since the fluxes and spectra vary tremendously with angle and distance.

The most significant complication is the considerable increase in flux and hardening of the spectrum from PuO_2 with elapsed time since fuel processing, due primarily to the build-up of daughter products from the contaminant isotope ^{236}Pu (SPS 37-59, Vol. III, pp. 112–115). Since there is no way of knowing in advance the age of the fuel at the time of launch, experimental measurements will have severely limited applicability. One alternative to experimental measurements is to utilize analytic methods, and the Monte Carlo techniques employed for this study are among the most powerful, efficient, and accurate ways of mapping these radiation fields to the required detail.

This study represents a first iteration analysis in that only a bare fuel capsule, not surrounded by the generator, is considered. The far more complex geometry which includes the generator is presently being set up together with the major structural features of the spacecraft. The work discussed here, however, is meant to represent a worst-case situation in order to place upper limits on the expected dose rates and levels as early as possible.

Even so, the resultant dosages and fluxes are relatively small, and should present little difficulty as far as shielding is concerned. Results indicate 180-day accumulated gamma dosages from two such capsules of less than 8 rads, even in the worst cases considered (assuming 5-yr-old fuel at launch), and less than 1 rad for some subsystems under more favorable conditions. Neutron dosages range from 3×10^8 to 16×10^8 neutrons/cm^2 for 180 days.

b. Basic assumptions. The fuel capsule chosen for analysis is a 675 W(th) $^{238}PuO_2$ SNAP-19 type of intact reentry heat source (IRHS), as shown in Fig. 1. This capsule is designed for the microsphere fuel form, the container consisting primarily of tantalum and Haynes-25 alloy, as called for in the SNAP-19 design for the *Nimbus* spacecraft. The actual *Viking* heat sources, however, will most likely be constructed of refractory metals and possibly contain the solid-solution fuel form. However, since specific capsule designs are not yet available, and since radiation attenuation within the source is due almost entirely to the self-shielding of the fuel, depending only slightly upon the thin-walled container, the SNAP-19 design was used, and should yield results in very close agreement with actual flight model sources. A more detailed analysis including the generator could utilize the actual capsule design once this becomes available.

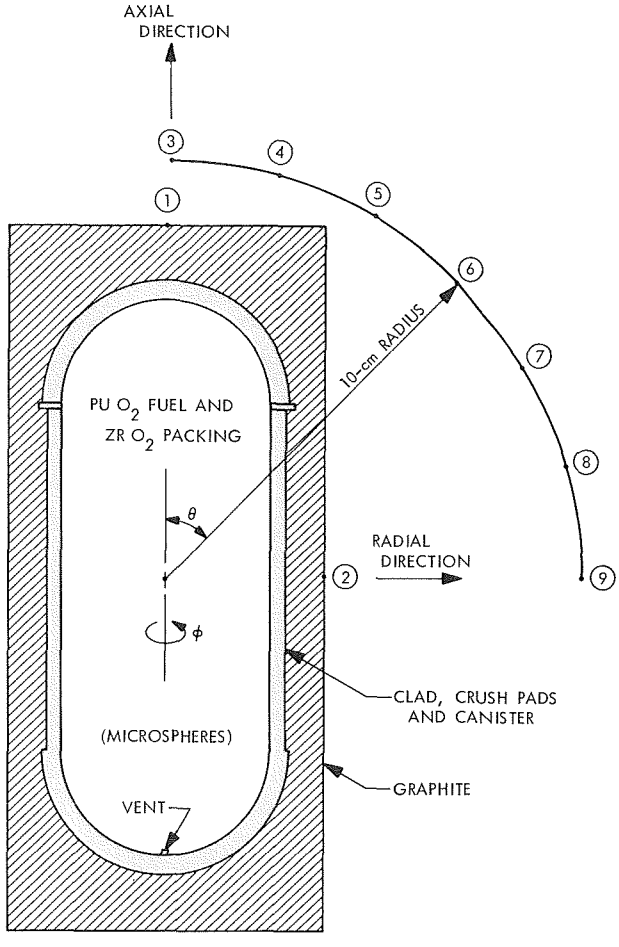

Fig. 1. 675 W(th) intact reentry heat source showing inner mapping points

Gamma-ray source spectra for nominal composition PuO_2 for three fuel ages, 0, 1, 5 yr are those of Gingo (SPS 37-56, Vol. III, pp. 128–132). Neutron sources are also due to Gingo, and include contributions from the $^{18}O(\alpha,n)^{21}Ne$ reaction, spontaneous fission, (α, n) reactions with other light elements present as contaminants, and induced fission neutrons. Changes with time of the neutron fluxes and spectra are quite small for the periods of time of interest here and have, therefore, not been taken into account.

The Monte Carlo code used to perform the calculations—RAMPARTS—is a highly improved and expanded version of the well-known FASTER code. It utilizes "importance functions" to achieve far better statistics than straight Monte Carlo simulation would for a comparable number of particle histories. The basic technique is to sample heavily those events which are most likely to contribute significantly to the results, while only lightly sampling the others. For this particular study, high-energy source particles are considered to a disproportionately large extent (since they have the best chance of eventually escaping from the capsule), while the initially low-energy particles, which will most likely be entirely absorbed and made no contribution to the fluxes exterior to the capsule, are sampled only slightly. The results are, of course, renormalized to the actual source spectrum after all calculations are complete.

Angular variables are biased as well, the technique used for this analysis being to bias for particles scattered into a wide-angle cone aimed toward a distant "preferred point." In this way the same particle history may contribute to the results for several detector points at different distances, again allowing more efficient operation on the computer. This, together with the unique feature of carrying all energies along simultaneously on each history, allows highly accurate results for many histories with a minimum of computer time.

Twenty-three detector points were used to make the maps, the first nine of which are shown on Fig. 1. The other fourteen were arranged into two arcs, one at 50 cm, the other at 100 cm, with points every 15 deg over the 90-deg arc. Since the capsule has ϕ symmetry and midplane reflection symmetry (except for the trivial

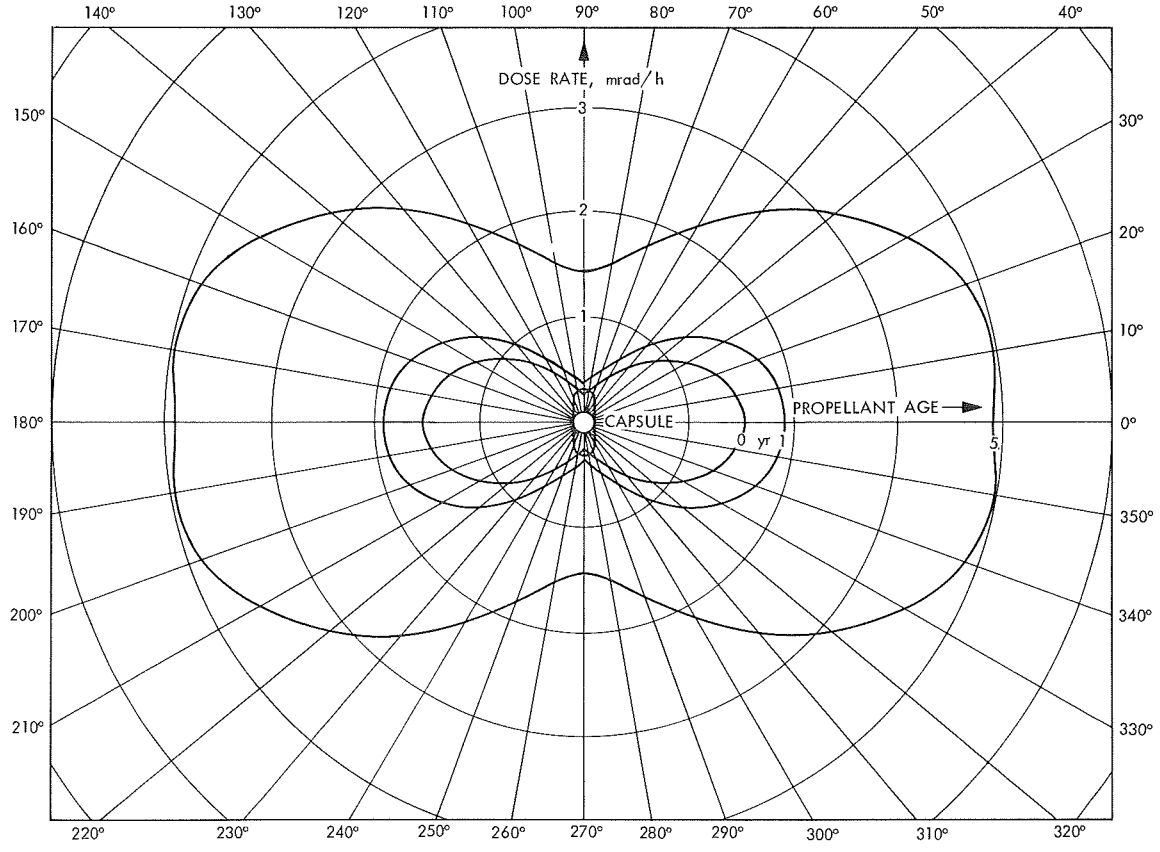

Fig. 2. Gamma ray dose rates for intact reentry heat source 100 cm from capsule center

influence of a washer and the helium vent), these points are sufficient to yield a complete map. Inverse square extrapolation beyond 100 cm is valid for greater distances for this small a capsule.

These flux and dose rate maps are then used to determine 180-day accumulated dosages at various orbiter subsystems. To do this, it is necessary to know the location and orientation of the RTG's within the lander. The lander will contain two RTG's, oriented parallel to, and probably symmetric with, the axis of the spacecraft. The orientation of the plane through the RTG's relative to the orbiter has not yet been established, however. Therefore, it is assumed that a single fuel capsule with twice the above flux levels is situated on-axis within the lander, as close to the orbiter as possible. Approximate angles and distances to various orbiter subsystems were then scaled from several blueprints of proposed orbiter designs. More accurate locations, both for orbiter subsystems and for the RTG's, should be available for future studies that could also consider the structural attenuation and scattering, which may be considerable.

c. Results. Dose rates and number flux determinations by detector point for gamma rays and neutrons were made. Angles were measured from the capsule axis, distances from the geometrical center. These values are plotted for the 100-cm points in Figs. 2 and 3. Note the significant angular dependance due to self-shielding, particularly for the gammas.

For the given input assumptions, the code gives errors to the gamma ray values of $\pm 12\%$, and the neutrons are within $\pm 7\%$. This is a little misleading, however, since the "preferred point" technique used to produce these results imparts the same absolute error to each point, i.e., all points are either high or low by exactly the same percentage. Thus, even though the absolute values are only accurate to the above percentages, the shape of the curves is not distorted.

Neutron and gamma ray spectra were determined for all detector points. Considerable attenuation of low-energy gammas in the axial case, as compared to the radial, was due to the self-shielding. An enormous build-up with age of the 2–3 MeV energy group (due to

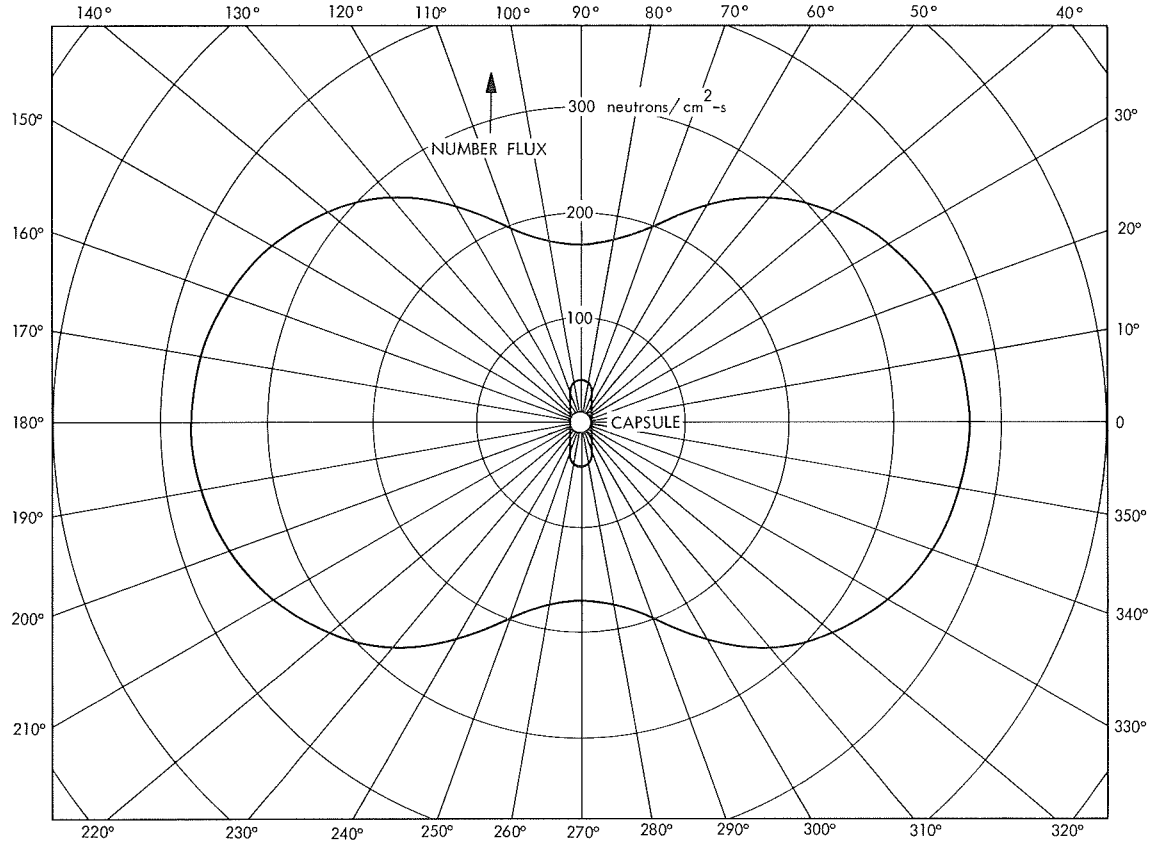

Fig. 3. Neutron number fluxes of the intact reentry heat source 100 cm from capsule center

^{208}Th, a daughter in the ^{236}Pu decay chain) is also quite evident for the gamma rays.

Figures 4 and 5 give gamma ray dose rate versus distance for the radial and axial directions, respectively; Fig. 6 compares axial and radial neutron fluxes.

Table 1 is a summary of the 180-day accumulated dosages for several orbiter subsystems. The distances given are all greater than 100 cm, and inverse square extrapolation was utilized to determine the radiation levels. The three gamma ages given represent age at launch, the build-up over six months having been considered in arriving at the tabulated values. As mentioned earlier, the gamma results are all quite small for permanent damage considerations, and should pose little problem to spacecraft designers. The neutron levels are, however, high enough to cause some concern and should be investigated in more detail.

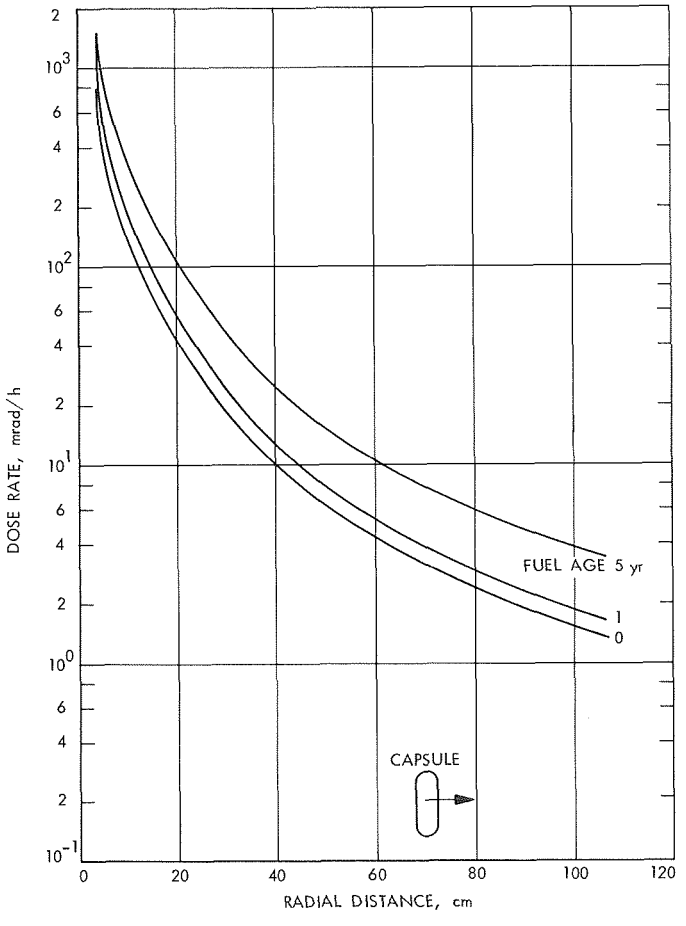

Fig. 4. Gamma dose rates for intact reentry heat source in the radial direction

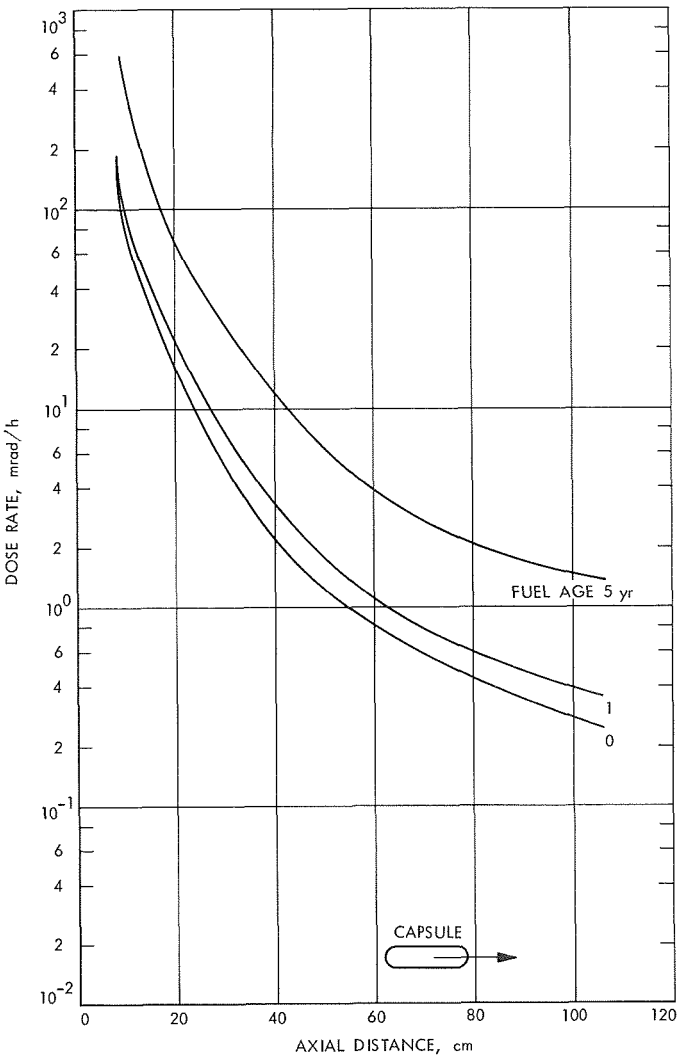

Fig. 5. Gamma dose rates for intact reentry heat source in the axial direction

2. Orbiter Power Subsystem

a. Power requirements. Periodic surveys of subsystems using power have resulted in a large increase in power supply requirements over those shown for the baseline design (SPS 37-56, Vol. I, pp. 42–47). The significant power changes are: A three-to-one increase in orbiter thermal control; and, an eight-to-one increase in lander power. The orbital thermal increase combined with some minor increases of other subsystems is reflected in Fig. 7. At the present time, as shown, the critical period for solar panel sizing now occurs during a battery charging and science playback mode. This is a change from the original baseline design where the solar panels were sized to the power required at the end of 90 days in orbit when the spacecraft is at the greatest distance from

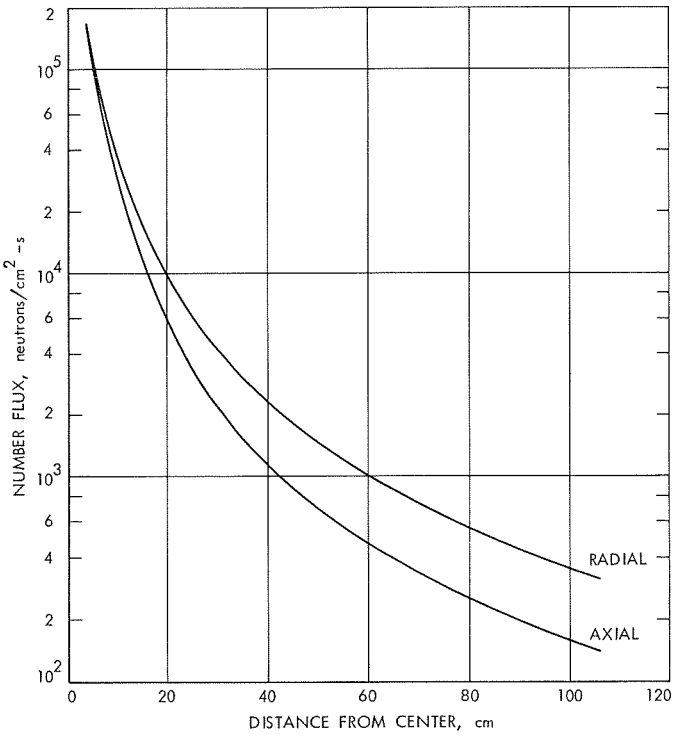

Fig. 6. Comparison of radial and axial neutron number fluxes of the intact reentry heat source

the sun. Also, a 60-min sun occultation mode (battery operation only) has been added, which occurs immediately following an orbit insertion maneuver.

b. Solar panel. During this reporting period, tradeoff analyses conducted have indicated that a 14-mil 2 × 2-cm cell represents the best tradeoff of power, weight, flight experience, and panel development risks. Analysis of the latest proton radiation model indicates that 6-mil-thick solar cell coverglass will supply sufficient radiation protection to 2-Ω-cm N-P silicon solar cells under the new levels specified. The new estimated radiation levels place the performance of the 2-Ω-cm N-P solar cell slightly above the threshold at which damage to the cell is likely to occur. If the anticipated radiation levels should increase in the future, reassessment of the coverglass thickness will be required. The reduction in specific performance due to the new estimated radiation levels has improved the baseline performance to 4.4 W/ft^2 at arrival (March 20, 1974) and to 4.2 W/ft^2 after 90 days in orbit. JPL has had previous experience in the application of 6-mil coverglass and does not anticipate any problem areas associated with its use. Previous experience includes the *Ranger*, *Surveyor* and *Mariner* programs (with the exception of *Mariner* Mars 1969 and 1971 which use 20-mil quartz coverglass). By selection of the 6-mil coverglass an approximate 18-lb weight savings can be achieved in the baseline design.

c. System operation and distribution. A preliminary functional block diagram of the *Viking* orbiter power subsystem is shown on Fig. 8. Unregulated dc power is provided to the lander with a command for turn-on and turn-off. Tentative assignment of all subsystem loads to the distribution network are also shown.

Two *Mariner* Mars 1971 battery chargers are provided for parallel trickle charging (low rate) during the transit period to Mars. In addition, high-rate charging of the batteries in a sequential mode of operation only, is also provided. Battery charging may also be commanded to turn on and off.

3. Orbiter Thrust Vector-Control System

a. Introduction. The thrust vector-control system or autopilot provides attitude control during engine burns for the midcourse maneuvers, orbit insertion maneuver, and orbit trims. This is accomplished by mounting the engine in a gimbal system as shown in Fig. 9. The engine is a modified version (RS-28) of the long-burn duration

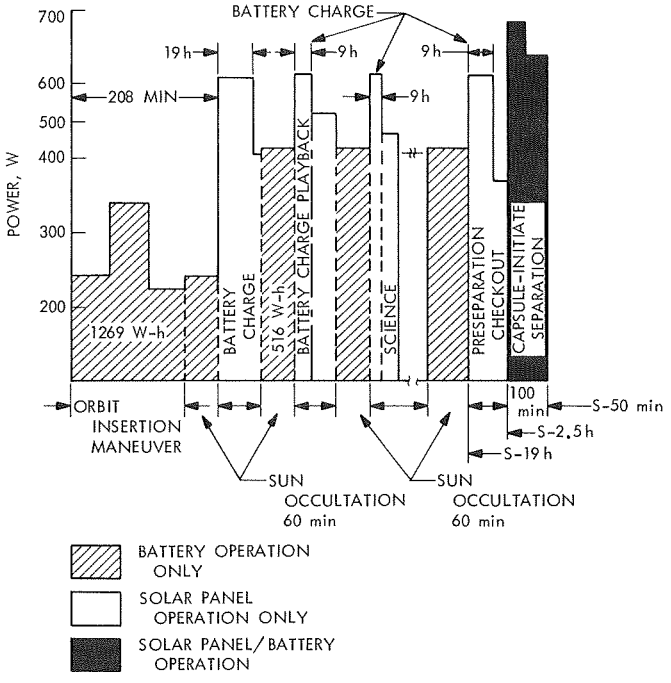

Fig. 7. *Viking* orbiter system preliminary power profile for orbit insertion maneuver, sun occultation, preseparation checkout, and capsule initiate separation

Table 1. 180-Day accumulated dosages

Subsystem	Minimum distance, cm	Angle, deg	Neutrons/ $cm^2 \times 10^6$	Gamma, mrad		
				0 yr	1 yr	5 yr
Inertial sensors						
Gyros	230	38	785.0	1191	1742	4408
Electronics	230	38	785.0	1191	1742	4408
Celestial sensors						
Stray Light Detector	200	35	1010.9	1458	2114	5510
Canopus Sensor	200	35	1010.9	1458	2114	5510
Sun Gate	220	56	1057.2	2169	2847	6260
Cruise Sensor	230	61	1002.5	2187	2856	6140
Acquisition Sensor	420	75	320.9	788	986	2010
Radio-frequency subsystem	210	29	825.2	1125	1573	4444
Science						
Platform (worst case)	130	0	1555.2	1645	2231	7892
TV	215	31	820.9	1157	1624	4358
IR mapper	195	21	830.3	1049	1474	4414
H_2O detector	195	21	830.3	1049	1474	4414
Electronics	210	29	825.2	1125	1573	4444
Actuators						
Jet valves	420	75	320.9	788	986	2010
Batteries	235	38	751.9	1197	1670	4221
Solar panels						
Inner edge	210	60	1195.5	2556	3364	7308
Outer edge	420	75	320.9	788	986	2010

Rocketdyne RS-14 300-lbf liquid bipropellant engine. The engine and gimbal system are located on the z (roll) axis with the engine pointing in the $-z$ direction. The gimbal control system positions the engine through the use of two linear actuators aligned with the pitch and yaw directions. This engine rotation capability allows the autopilot system to point the thrust vector through the spacecraft center of mass. With only this system, control cannot be effected about the roll axis. Since swirl in the exhaust gases produces some torque, additional control must be provided for roll stability. Roll control is accomplished using the cold-gas roll-attitude-control channel. This method of providing thrust vector control is identical to that used on the *Mariner* Mars 1971 spacecraft. However, the structural properties of the *Viking* spacecraft are quite different from the *Mariner* Mars 1971 spacecraft, and a complete detailed analysis is required to obtain the design parameters to meet the system requirements.

b. Autopilot mechanization. A single-axis block diagram of the autopilot is shown in Fig. 10. The autopilot electronics consists of the following:

(1) Pitch and yaw preamplifiers.

(2) Pitch and yaw guidance amplifiers.

(3) Motor gimbal pre-aim circuitry.

(4) Pulse-width-modulated gimbal servo amplifier.

(5) Linear variable differential transformer.

(6) 6.0-KHz regulated power supply.

In Fig. 10, the function of the path guidance circuit is to provide automatic compensation for CG offset errors and migration. This can be particularly critical for the long insertion burn. The function of the pre-aim circuitry is to bias the gimbal servo null point approximately through the CG prior to motor ignition. This eliminates

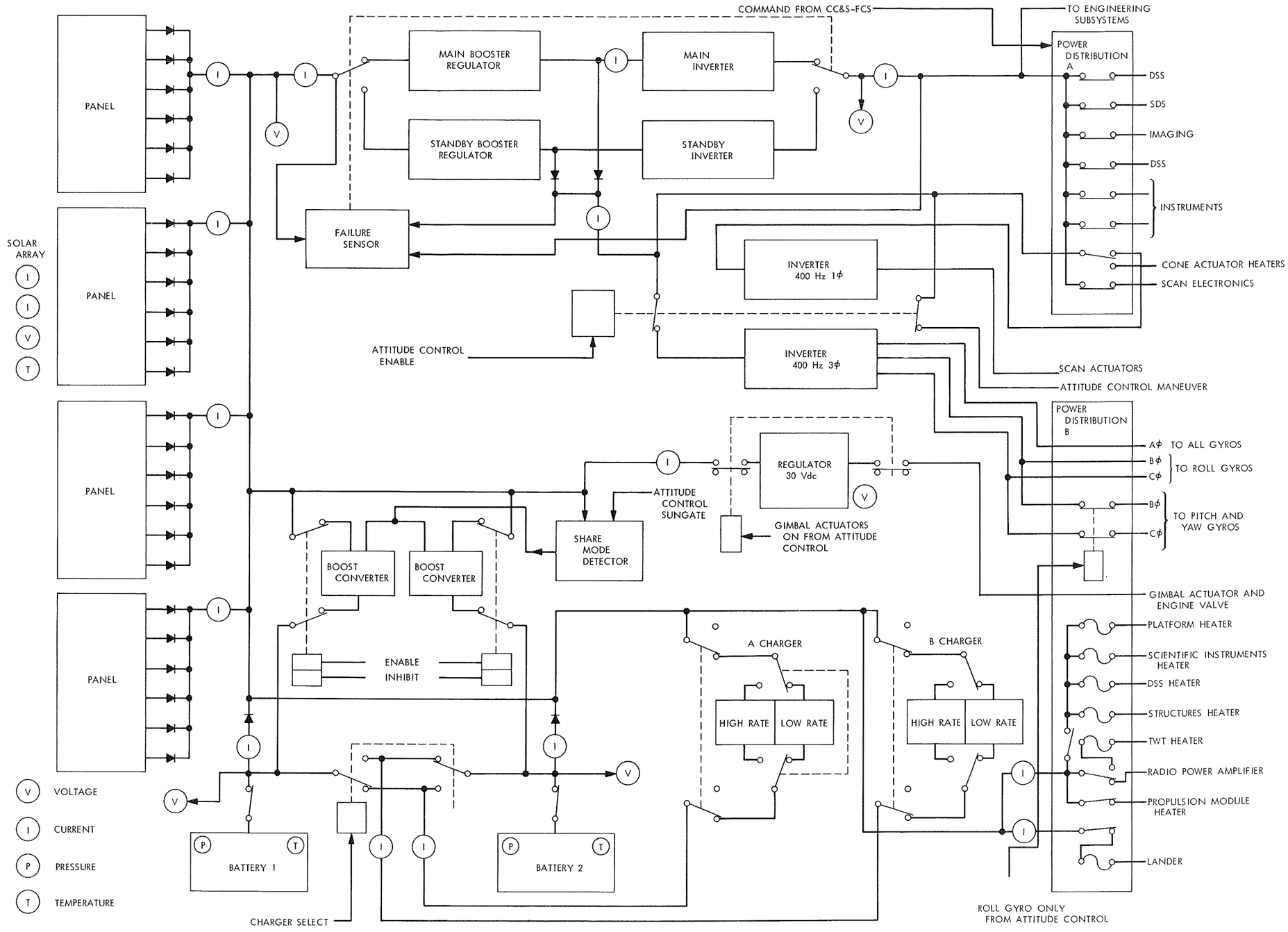

Fig. 8. *Viking* orbiter preliminary power subsystem

Page intentionally left blank

large gimbal motion transients at motor ignition. In addition, the pre-aim reduces motor thrust vector to CG misalignments that could cause pointing errors during the short orbit-trim burns.

After completion of the commanded turns, which orient the spacecraft so that the engine is in the proper inertial attitude for the velocity change maneuver, a signal for motor ignition causes the motor burn switch to make two changes in the autopilot and attitude-control system: (1) the pitch and yaw gas systems are disabled to prevent wasting large amounts of cold gas during the burn, and (2) the path guidance circuits are enabled. As previously stated, these circuits provide compensation for CG alignment errors and migration

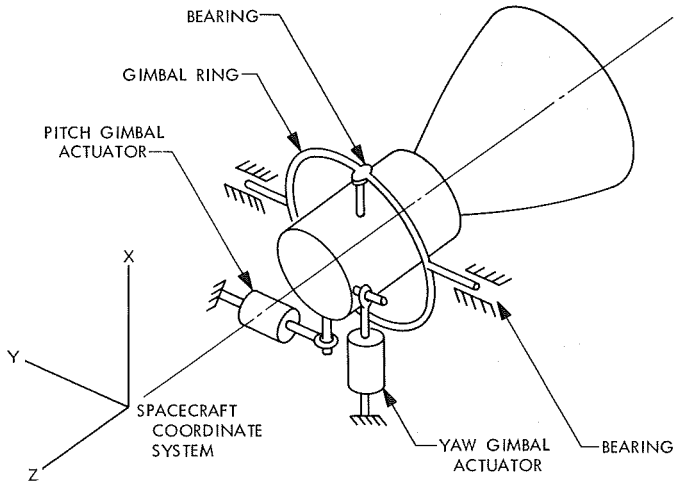

Fig. 9. Engine and gimbal mounting arrangement

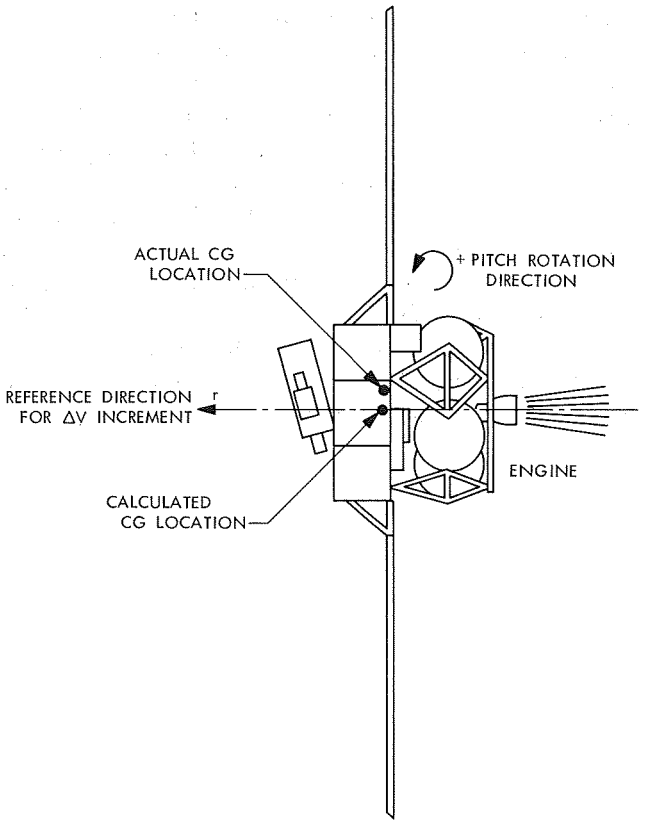

Fig. 11. Spacecraft attitude at motor ignition

during the burn. The changes are completed simultaneously with motor ignition. At motor ignition, the spacecraft is in the position shown in Fig. 11. The commanded turns have been performed so that, excluding turn errors, the spacecraft z axis is aligned with the

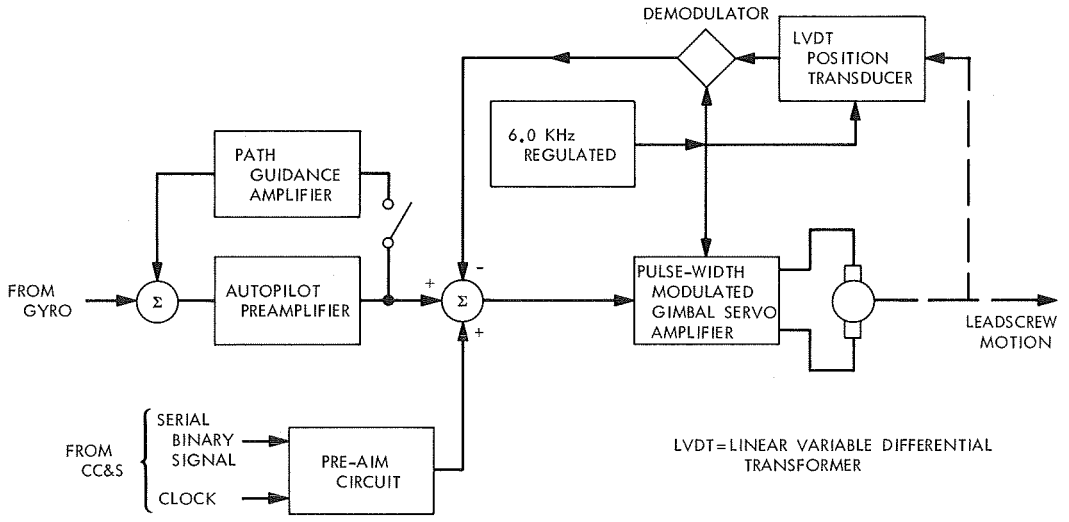

Fig. 10. Autopilot block diagram with path guidance and pre-aim circuit

vector r, the inertial reference direction for the ΔV increment. The gimbal actuators are at null (or slightly off due to roll gas system limit cycling) and the engine is aligned with the calculated position of the CG. Due to errors in the CG determination, the calculated position does not coincide with the actual CG location. Figure 12 shows the evolution of the thrust–CG relationship during the burn. Here the first sketch, showing the conditions at ignition, is exactly Fig. 11 with the spacecraft outline removed for clarity. This shows the thrust vector in the proper reference direction, but misaligned with the CG. This produces a negative torque on the spacecraft. The second sketch shows the resulting transient. As the torque rotates the spacecraft in the negative pitch direction, the pitch gyro senses the error θ between the reference direction r and the z axis, producing a positive output voltage. This voltage is filtered by the autopilot and used to drive the gimbal servo. The engine is now rotated until the angle ϕ is sufficient to pass the thrust vector through the CG. At this time the engine thrust vector is $\theta + \phi$. Without path guidance, the spacecraft would maintain this attitude during the entire burn. However, the path guidance circuit senses the gimbal command voltage and feeds it back to the autopilot input, through an appropriate filter, as shown in Fig. 13. This positive feedback causes the angle ϕ to increase very slowly in

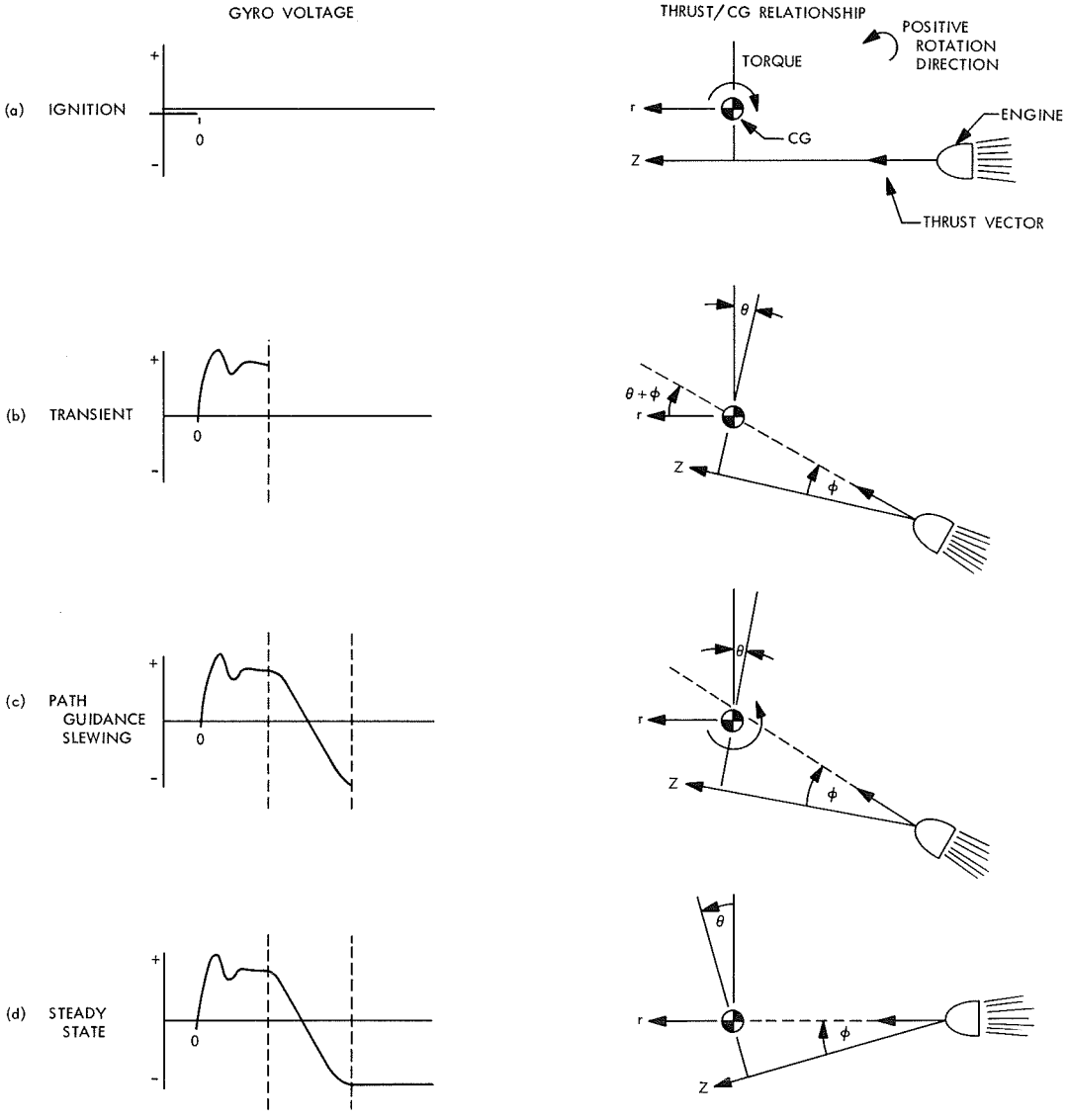

Fig. 12. Thrust CG relationship during motor burn

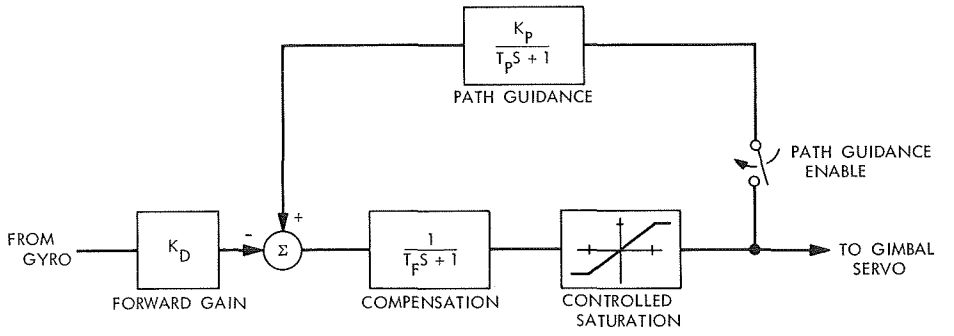

Fig. 13. Path guidance autopilot block diagram

magnitude. The result on the spacecraft is a positive torque which slews the attitude as shown in Fig. 12c. The gains in the path guidance loop are set so that when the gyro error signal exactly cancels the positive feedback, the attitude of the spacecraft is such that the thrust vector is aligned with the desired reference vector r. Even though there is positive feedback in the path guidance minor loop, overall stability of the autopilot is not affected. Engine shut-down occurs when a linear accelerometer indicates that the required ΔV magnitude is reached. At this time the motor burn switch disables the path guidance and enables the pitch and yaw gas systems. Attitude control is now returned to the gas system.

c. Autopilot accuracy. When the spacecraft is at a steady-state condition during the engine burn, the engine is aimed at the CG, and without path guidance, makes an ϕ with the z axis as shown in Fig. 14. Since the angle is commanded by the autopilot, it is a known source of thrust vector error. Path guidance corrects for this error by setting the steady-state gain between gyro input and gimbal angle equal to -1. For stability, the gimbal must point the engine through the CG, and thus the attitude angle of the spacecraft must be the negative of the gimbal angle. In theory, then, the thrust vector will be exactly in the inertial reference direction except for the mechanical alignment errors of the engine. The mechanical alignment errors which cannot be corrected for are: α_T, the angular error between the actual thrust and the engine geometric thrust axis, and α_E, the engine angular alignment error.

Referring to the autopilot loop in Fig. 13, it is seen that the path guidance feedback modifies the steady-state gain. There is an associated lag T_P that is used to prevent this feedback from degrading the transient performance of the system. The feedback K_P is set by the relation

$$K_P = 1 + K_F$$

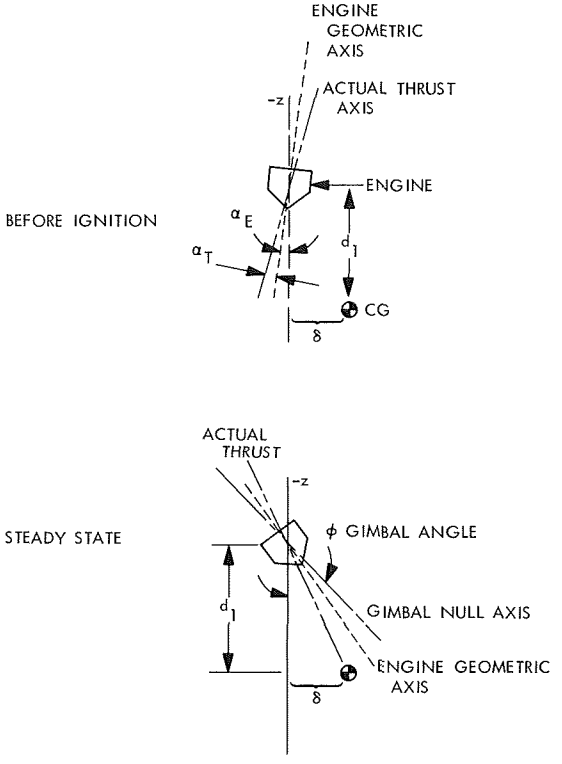

Fig. 14. Path guidance steady-state error

and

$$K_F = K_G K_D K_A$$

where

K_G = gyro position scale factor

K_D = autopilot forward loop gain

K_A = gimbal servo gain

The steady-state error is

$$K_F\theta + K_P\phi = \phi = \alpha_T + \alpha_E + \frac{\delta}{d_1}$$

where

d_1 = lever arm

δ = CG offset

If K_P were exactly its nominal value, the steady-state error would be

$$\alpha_{ss} = -\alpha_T - \alpha_E$$

However, due to thermal variations in K_G and the gimbal servo linearity, and the inability to perfectly match the gains such that the steady-state gain between gyro input and gimbal angle is identically -1, an additional error is introduced. The steady-state thrust vector error can be approximated by

$$\alpha_{ss} = -\alpha_T - \alpha_E + \frac{\Delta K_F}{K_F}\left(\frac{\delta}{d_1}\right)$$

where ΔK_F represents the aforementioned gain variations. $\frac{\Delta K_F}{K_F}$ is approximately 0.1 in the worst case and 0.06 3σ.

d. Autopilot gain considerations. The basic autopilot system is identical to the *Mariner* Mars 1971 system. The most significant difference that the autopilot must be able to cope with is the much larger variation in spacecraft inertias and engine lever arm. The autopilot loop gain is given by

$$K_{AP} = \frac{K_G K_D K_A T\, d_1}{I}$$

In the case of the original baseline spacecraft configuration, the spacecraft pitch and yaw inertias undergo a 6.6-to-1 change, and the engine lever arm undergoes a 2.33-to-1 change between the beginning of orbit insertion and the completion of capsule separation phase. The net result is about a 3-to-1 change in autopilot loop gain. There are several criteria for establishing the correct loop gain. With regard to the *Viking* spacecraft, the most important criterion is establishing the gain so that a low-frequency instability will not result. The low-frequency instability is a secondary effect of path guidance on the system. The path guidance loop introduces a lower gain limit into the system stability criteria. In addition to this, normal autopilot operation will exhibit low-frequency limit cycle behavior due to the inherent stiction thresholds in the gimbal actuators. The magnitude of these oscillations is determined by the threshold voltage necessary to overcome the gimbal stiction and the gimbal servo loop gains. The effect of path guidance is to raise this limit cycle frequency so that the period is approximately equal to T_P, the path guidance feedback time constant. Normally, this occurs without a change in amplitude. If the autopilot loop gain is maintained above the critical lower gain, the overall effect in system behavior is negligible. To maintain adequate stability margins, the autopilot loop gain must be switched at or just before capsule separation. This is necessary to ensure proper autopilot performance for any subsequent orbit-trim maneuvers. This gain switching could easily be accomplished by a single solid-state relay closure that is initiated at capsule separation. The gains would be changed such that the loop gain is maintained at the proper level and the proper path guidance relation is maintained.

C. Engineering Mechanics

1. Design Modifications and Criteria

Preliminary design studies have continued during this report period. Two significant changes have been in the *Viking* orbiter propulsion module and in the orbiter-to-lander adapter.

a. Propulsion module. The propulsion module previously described consisted of a four-tank cluster of two fuel and two oxidizer tanks. There were also four small spherical tanks of high-pressure nitrogen grouped near the rocket motor. The nitrogen was used as a pressurant feed for the propellants. The present configuration is a much simpler and more economical arrangement of two propellant tanks and two pressurant tanks. The pressurant, however, has been changed to helium to save weight.

b. Orbiter-to-lander adapter. The orbiter-to-lander adapter was initially shown as a truss structure from four points on the orbiter to four points on the lander-capsule system. Subsequent to the selection of the lander design it became apparent that a three-point support of the lander was more appropriate. With the change to the two-tank propulsion module even the four mounting points on the orbiter were shifted slightly. These new considerations were incorporated into a four-to-three-point adapter.

c. Loads analysis. Several structural design philosophies have been clarified and have met agreement. It became clear that a much lighter structure would result if the design were based on estimates of the flight transient loads rather than sustained sinusoidal loads traditionally encountered in the environmental qualification

tests. This departure from past practices requires a new definition of the qualification test sequences. It now appears that flight load will be the governing factor in the low-frequency environment, but the more traditional approach will be retained for the mid and high-frequency environments.

As a result of this approach most of the weight advantage can be realized with a minimum departure from established practices. The definition of the transition from the low-frequency criteria to the midfrequency will depend on the quality of the available data. Initial estimates range from 20 to 40 Hz.

Results from a preliminary loads analysis using a very simple model of the *Viking* spacecraft have been applied as forcing functions to a simplified dynamic model of the *Viking* orbiter. This analytical model now consists of only 180 elements with 248 static degrees of freedom and 128 dynamic degrees of freedom but provides a sufficient basis for the preliminary design of the orbiter structure. As more information becomes available, this model will be improved and used as the basis for the detail design of the orbiter hardware.

D. Propulsion

1. Orbiter Propulsion and Pyrotechnics

a. Propulsion subsystem. The function of the *Viking* orbiter propulsion subsystem is to provide the necessary velocity increments for the in-transit trajectory corrections, an orbit-insertion maneuver at Mars and the orbit-trim maneuvers. The selected subsystem design is an outgrowth of the *Mariner* Mars 1971 propulsion subsystem technology.

Early in the orbiter design a baseline propulsion design was established making maximum use of *Mariner* Mars 1971 technology and hardware. This design was a pressure-fed multistart constant-thrust storable bipropellant propulsion system utilizing nitrogen tetroxide (N_2O_4) and monomethylhydrazine (MMH) operating at a mixture ratio of 1.55:1. The propulsion subsystem was designed as a complete modular assembly which could be mated or demated from the remainder of the orbiter as required. A description of the baseline configuration was covered in SPS 37-59, Vol. I, pp. 42–45.

Since the last report a detailed analysis of a two-tank configuration was completed. Based on the results of the study it was decided to implement the two-tank configuration. By going to the two-tank configuration the packaging arrangement of the entire orbiter was improved and there was some simplification of the propulsion subsystem because of the deletion of the propellant migration valves, two propellant tanks, and two pressurant tanks. The guidance and control capability was unaffected by the change, even though there is a lateral shift in the spacecraft CG during propulsion subsystem operation (particularly orbit insertion) because of the difference in the masses of the two propellants. Also, there appears to be a slight savings in mass. The new propellant tank size is 3 ft in diameter by about 5 ft in length. A schematic of the two-tank configuration is shown in Fig. 15.

With the establishment of the two-tank configuration, feed system layouts were started using basically the *Mariner* Mars 1971 propulsion feed system components. The major-component type modification being considered is in the area of the isolation valve package. On *Mariner* Mars 1971 this function is being performed by a series of pyrotechnically actuated valves. Because of the desire for several orbit changes, the limitations on flexibility of the squib-actuated valves are being evaluated. A review of off-the-shelf solenoid actuated valves was conducted, and as a result two latching solenoid actuated valves were purchased. These valves were originally developed for *Gemini* and *Manned Orbiting Laboratory*. A testing program will be implemented to determine the capability of the valves to meet *Viking* requirements. Another change under consideration is the pressure transducer type. Because of the problems of procuring potentiometric-type transducers for the *Mariner* Mars 1969 and 1971 spacecraft, a study is being made of the use of a strain-gage type transducer for the propulsion subsystem.

b. Pyrotechnic subsystem. The *Viking* orbiter pyrotechnic subsystem is based on proven techniques and design philosophy employed in previous *Mariner* spacecraft subsystems. Improvements in circuitry and components that enhance reliability will be incorporated. The design is essentially that of the *Mariner* Mars 1971, modified only to the extent required to accommodate the increased propulsion events. A description of the subsystem is covered in SPS 37-59, Vol. I, pp. 44–45.

During this period the effort included an examination of the *Mariner* Mars 1971 pyrotechnic switching unit (PSU) to understand which portions of the unit will be usable for *Viking*, and a preliminary assessment of the

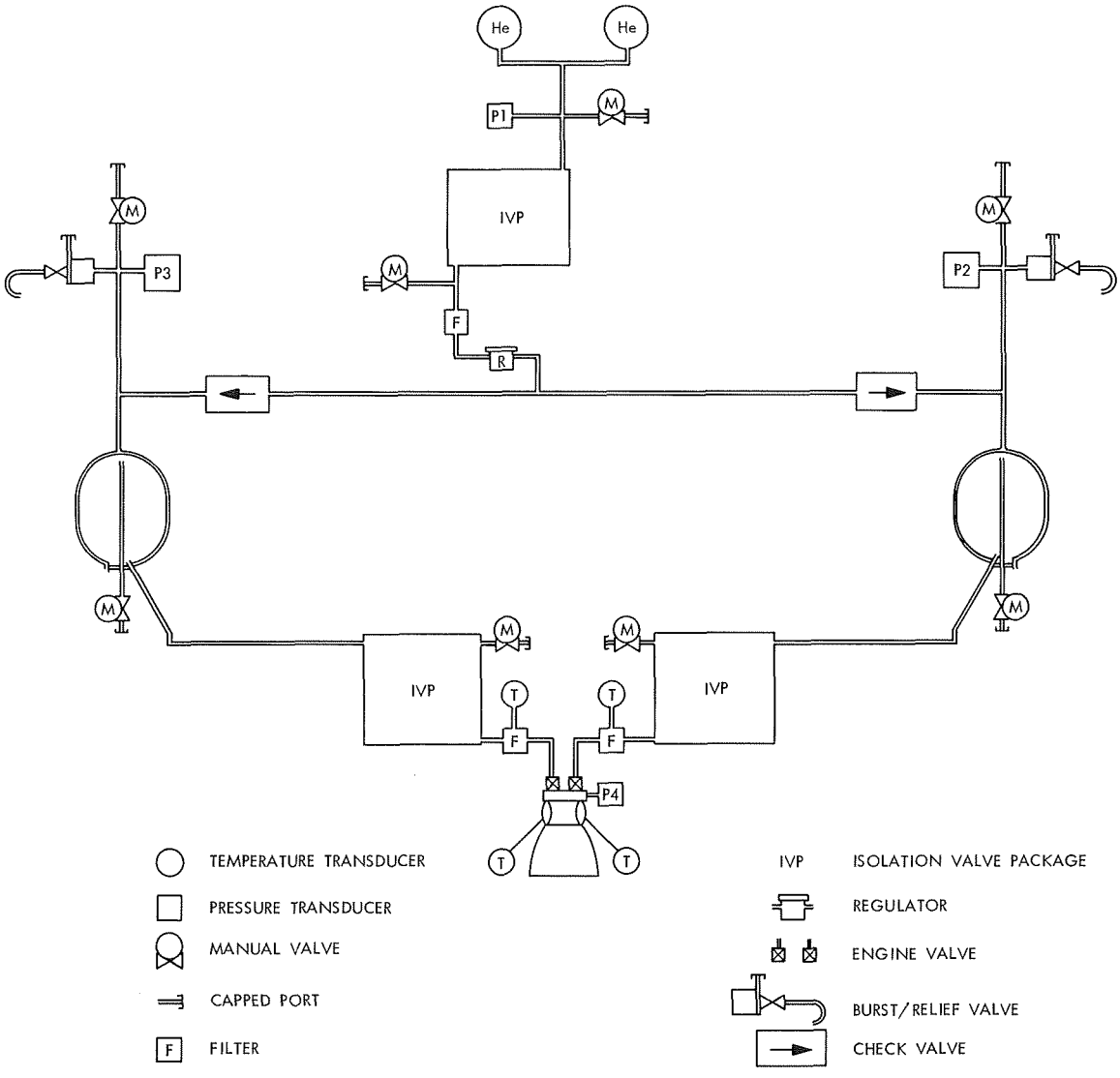

Fig. 15. Two-tank configuration for propulsion subsystem

circuitry needed for the propulsion solenoid actuated isolation valve. Because of the increase in the number of functions over those of *Mariner* Mars 1971, the physical size and the number of connector pins have increased. As a result, three approaches to the problem are being evaluated: (1) Reevaluation of the baseline requirements to see if certain functions could be combined or eliminated, (2) Use existing PSU and design a second unit to handle the overflow, and (3) Modify or redesign the *Mariner* Mars 1971 PSU to accommodate the increased requirements. The final choice of approach will depend on cost, weight, and schedule tradeoffs.

A preliminary evaluation of potential explosively actuated devices for *Viking* requirements has been started. The initial indications are that the pinpuller used on *Mariner* Mars 1971 may be used directly for the antenna unlatch functions. The major change will be the new type of release device needed for spacecraft separation and for separation of the lander aft bioshield support structure. Because of the magnitude of the stresses at the respective attach points, it may not be possible to utilize off-the-shelf hardware. The study of this device and the requirements placed on this device is continuing.

2. Evaluation of Phosphate-Treated Ammonium Perchlorate in Saturethane Propellants

It has been found that the ability of Saturethane propellants to withstand the 275°F 53-h dry-heat

sterilization cycles without evidence of decomposition is dependent on the manufacturing lot of ammonium perchlorate (AP); however, to date, the reason for this variation is unknown. Personnel at Langley Research Center during independent studies on propellant burning rate observed that the low-temperature decomposition of neat AP was reduced when it was recrystallized from water solution in the presence of diammonium phosphate. The extension of this work was to determine if the observed improved stability would also be found when the phosphate treated-recrystallized AP was utilized in a Saturethane solid propellant. Saturethane propellant formulations, for which comparison data were available (Ref. 1), were selected for the evaluation. The result of the evaluation is that no improvement in sterilizability has been observed when the phosphate-treated oxidizer was utilized.

a. AP preparation. The AP used in this evaluation was supplied to JPL by Langley Research Center in four separate shipments. Each sample except the first, which was recrystallized in the laboratory, was prepared by recrystallizing commercial grade AP containing 0.2% tricalcium phosphate plus 4% on total solids of diammonium hydrogen phosphate or trisodium phosphate from a water solution in a 20-gal solid propellant Day mixer. The AP was then filtered out, dried at 160°F, and sieve-separated before shipment to JPL.

b. AP analysis. The first two shipments of AP had moisture contents (0.2 to 0.3%) which would not permit mixing and curing of Saturethane propellants. Thus, the first lot was vacuum dried at 275°F. It was believed that drying the treated material at high temperatures (275°F) could have possibly degraded the AP before its incorporation into a propellant; however, it was difficult to reduce the water content to the acceptable 0.03% level by drying at temperatures less than 275°F. Table 2 shows the results of attempts to dry AP from the second shipment in a thin layer on a tray in a fresh-air oven.

Table 2. Ammonium perchlorate drying

Drying temperature, °F	Drying time, days	Moisture, wt %
170	62	0.072
190	62	0.068
220[a]	62	0.024

[a]It was observed that this sample for some unknown reason had turned to a light brown color after drying.

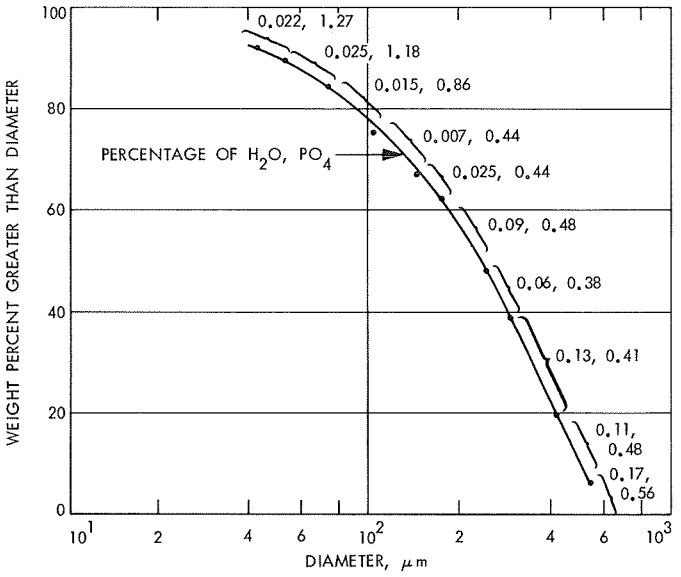

Fig. 16. Moisture, phosphate, and particle size analysis of phosphate-treated oxidizer

Further investigation revealed that the majority of the moisture was concentrated in the large crystals. Figure 16 shows the particle-size distribution of the second shipment of AP received. Tabulated on the figure are the weight percent of moisture and percent of phosphate as a function of particle size. The weight percent moisture is greater in the larger crystals, whereas the phosphate concentration is greatest in the small crystals. AP crystals less than 150 μm were dried easily on trays to less than 0.03% moisture. Thus, oven drying at 220°F and crystal particle sizes of less than 150-μ diameter were utilized for the evaluation.

c. Neat ammonium perchlorate stability. The stability of the neat AP is markedly improved by recrystallization with the phosphate as shown in Fig. 17. This figure shows the weight percent loss as a function of time at 278°F of the AP as received from the American Potash Company and of the same lot of AP recrystallized with the phosphate. The initial weight loss of the recrystallized AP may be due to moisture as separate analyses showed the moisture content to be 0.2%. These data indicated that the phosphate-treated AP utilized had good thermal stability as measured by oven weight loss; however, it should not be implied that the phosphate treatment alone caused this result, since other work (Ref. 1) has shown that recrystallizing AP from water (no phosphate) can also markedly improve its oven thermal stability.

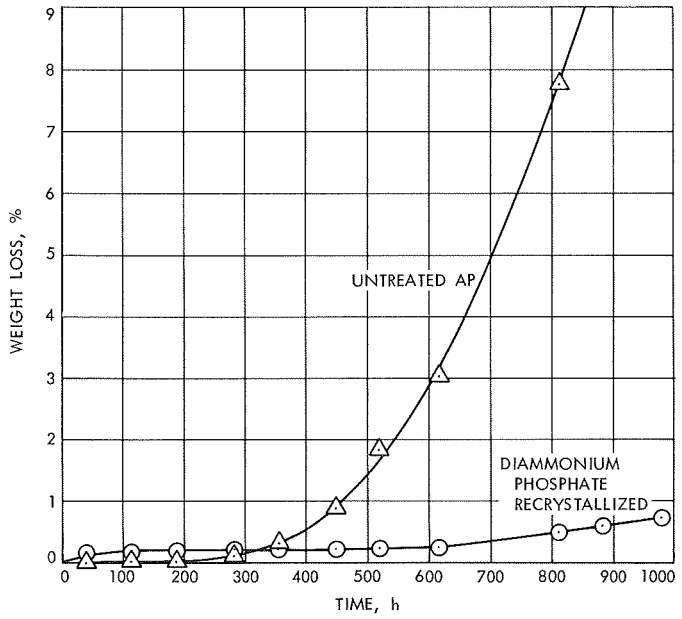

Fig. 17. Results of oven weight loss test of neat treated and untreated ammonium perchlorate at 278°F

d. Propellant stability. The propellant stability was tested in two different types of propellant. The first was nonaluminized low-modulus propellant with a 30% binder that could accommodate unimodal oxidizer. The second was a high-modulus propellant (high crosslink density in the binder) which contained 18% aluminum and 19% binder. Each formulation and batch used the identical lots of ingredients and mix procedures except for the AP.

Propellant stability was determined by radiographic analysis of 3-in.-dia by 3-in.-long solid cylinders. The appearance of small voids within the grain indicated failure. Some swelling usually occurred in the high-modulus propellants.

Table 3 tabulates the results of these tests. The 181-X propellant series contain 30% binder; the 212-X batches are high-modulus propellants. All batches were cured for 5 days at 220°F.

Batch 181-S19 failed during its first sterilization cycle (56 h at 275°F). The particle size of the AP used in this batch was quite large. The AP, as received, was ground with a mortar and pestle to less than 420 μm. It was then dried at 275° for 30 h under vacuum. Because of the severe drying procedure, it was felt that possibly the oxidizer was degraded before it was incorporated into the

Table 3. Results of propellant heat-sterilization cycles

Batch	AP shipment	Particle-size distribution, μm	Compound co-crystallized with AP	PO_4, %	Drying procedure	Moisture content, %	Physical properties after cure at 72°F		Number of 56-h cycles at 275°F (when voids were observed in radiographs)
							s_m	e_m	
181–S19	1	<420	$(NH_4)_2HPO_4$	1.2	275°F under vacuum for 30 h		—	—	1
181–S26	2	As received unground	$(NH_4)_2HPO_4$	0.5	160°F in fresh air oven for 40 h	0.2	Swelled during cure		—
181–S30	2	<150	$(NH_4)_2HPO_4$	1.0	220°F in fresh air oven for 16 h	0.012	183	76	1
181–S31	2a	Grind 100 <150	(Not recrystallized)	0	As received	0.014	168	73	4–5
181–S32	2a	As received	(Not recrystallized)	0	As received	0.014	106	68	2
181–S38	2	Grind 100 <150	$(NH_4)_2HPO_4$	1.0	220°F in fresh air oven for 16 h	0.012	152	76	2
181–S40	2	Grind 100 <150	$(NH_4)_2HPO_4$	1.0	220°F in fresh air oven for 40 h	0.008	216	97	2–3
181–S42	4	<150	Na_3PO_4	0.29	As received	0.023	163	55	1
212–S3	2a	As received	(Not recrystallized)	0	As received	0.014	294	25	1
212–S4	3	<150	$(NH_4)_2HPO_4$	1.4	As received	0.013	368	21	0
212–S5	4	<150	Na_3PO_4	0.29	As received	0.023	—	—	2

propellant. Thus, a second batch, 181-S26, which used AP which was dried at 160°F for 40 h, was prepared; however, the propellant swelled during cure due to the high moisture content of the AP.

All the remaining batches which contained recrystallized AP used AP which had been sieved through a 100-mesh screen (<150 μm). Batches 181-S30, 31, 32, 38, and 40 were prepared to test the effects of sieving, grinding, and recrystallizing the AP.

From these batches the following can be concluded: First, the most stable propellant used the parent (not recrystallized) AP lot which had been ground and then sieved to less than 150 μm. Secondly, sieving and then grinding the recrystallized AP (batches 181-S38 and 40) made slightly more stable propellant than that which used only sieved AP (181-S30). Batch 181-S42 used the fourth shipment of AP which was sieved and dried at Langley Research Center. This AP was co-crystallized with Na_3PO_4. Again the propellant failed during the first sterilization cycle.

The high-modulus batches were difficult to process, and there were casting voids (bubbles) in the charges. Batch 212-S3, which used the parent AP lot, failed after one cycle. Batch 212-S4 failed during cure. Batch 212-S5 survived one cycle but failed during the second cycle.

e. Conclusions. From the results of these few tests the parent AP appears to be as stable or more stable than the recrystallized-phosphate-treated AP in the Saturethane propellant system. For the neat AP the recrystallized-phosphate-treated AP is more stable in an oven environment than the parent material.

Reference

1. Robillard, C., *Development of Saturethane Propellants*, TR 32-1406, Jet Propulsion Laboratory, Pasadena, Calif., March 27, 1969 (Confidential).